applied sciences

MDPI

Article

Assessment of Spatio-Temporal Kinematic Phenomena Observed along the Boundary of Triaxial Sand Specimens

Yichuan Zhu [1,*] and Zenon Medina-Cetina [2,*]

[1] Civil & Environmental Engineering Department, Temple University, Philadelphia, PA 19122, USA
[2] Zachry Department of Civil & Environmental Engineering, Texas A&M University, College Station, TX 77843, USA
* Correspondence: yichuan.zhu@temple.edu (Y.Z.); zenon@tamu.edu (Z.M.-C.)

Abstract: This paper follows up on a reference paper that inspired MDPI's topic "Stochastic Geomechanics: From Experimentation to Forward Modeling", in which global and local deformation effects on sand specimens were fully described from high-resolution boundary displacement fields. This paper is supported by that study's experimental database, which is open to the scientific community for further study. This paper focuses on the analysis of this experimental study to investigate strain localization effects on a subset of tests included in this database. Strain localization is defined here as associated with the non-homogeneous deformation process occurring in elastoplastic materials, including sands. Many experimental and numerical studies have been conducted during the last two decades to explore the characteristics of localization effects on sand, and to determine how these contribute to the failure mechanisms of specific sands. Under a triaxial compression condition, localization effects have been studied mainly with regard to particle kinematics and translational strain of the specimen's displacement fields. However, to the best of the authors' knowledge, there has been no 3D experimental kinematic analysis performed on sands to study the localization phenomena that can directly relate the impact of a specimen's initial and boundary conditions to a failure mechanism during a triaxial test. In this paper, we introduce a full set of 3D kinematic operators under cylindrical coordinates to assess the boundary localization effects of deforming sand specimens under triaxial loading conditions. Furthermore, a set of experiments were carried out under varying experimental conditions to study the impact of variability in these localization effects. Results show that patterns of kinematic effects are quantifiable and can be used to assess likely failure-influencing factors, such as confining pressure, initial density, sample geometry, and sample heterogeneity, in the development of specific failure mechanisms. Spatio-temporal interdependencies between localization effects, such as the interactions between shear, expansion, and compaction bands observed during the specimen's shearing process, were also studied. We therefore hypothesize that the proposed framework will serve as the basis for quantifying the uncertainty associated with the development of localization effects over the boundary of sand-deforming specimens.

Keywords: sand specimens; kinematic analysis; triaxial compression test; localization effects; shear band; compaction band; expansion band

Citation: Zhu, Y.; Medina-Cetina, Z. Assessment of Spatio-Temporal Kinematic Phenomena Observed along the Boundary of Triaxial Sand Specimens. *Appl. Sci.* **2022**, *12*, 8091. https://doi.org/10.3390/app12168091

Academic Editor: Ricardo Castedo

Received: 6 July 2022
Accepted: 8 August 2022
Published: 12 August 2022

1. Introduction

Two reference papers precede this work: one introducing the supporting experimental database used to produce the analyses on localization effects discussed in this paper [1], and its companion paper, which presents the statistical analyses of the experimental database [2]. This paper introduces a study of strain localization in sand specimens, which is assumed to be associated with non-homogeneous deformation occurring in materials when they are subjected to compressive or tensile stress [3]. The accumulation of strain localization is frequently presented as a thin zone of intense deformation [4], such as shear, expansion, or compaction band, which encompass the main material responses once it is fully formed [5].

Since the onset and evolution of localization effects underlie soil mechanical failure processes, its study plays a key role in advancing the understanding of geomechanics, from its phenomenological behavior (global stress-strain responses) to fundamental physics (particulate interactions), to provide the best interpretation of the micro-deformation mechanisms associated with macro-deformation mechanisms observed in geo-structure behavior (e.g., foundations, dams, excavations, etc.).

The analysis of localization based on laboratory experimentation requires access to full displacement fields and to standard global (axial) measurements. The latter typically yield at best the averaged material response (global/axial stress-strain behavior), disregarding the occurrence of any localization effects. On the other hand, modeling of full displacement fields, including the use of the discrete element method (DEM) [6,7], has played an important role, owing to its ability to account for particle–particle interactions and granular morphology, thus enabling the strain localization to be revealed on the grain scale [8–12]. For example, Oda and Iwashita [12] used DEM to reveal the formation and collapse of column-like structures, parallel to the principal stress direction during the hardening and softening phases of a sample compressed under the plane strain condition. Further, the ability of DEM to directly measure particle contact maps and kinematics allows for inspection of nonaffine deformation features, including microbands [13], vortex structures [8,14], and translational/rotational behaviors of soil clusters [15,16], among other strain localization phenomena.

Some experimental efforts to measure full-field displacement fields, and to study grain-scale kinematics in particular, include the study by Hall et al. [17], who combined X-ray imaging and digital image correlation to study the three-dimensional translation and rotation of sand grains in a sand specimen. Based on this work, Andò et al. [18] further developed the 1D-Track technique, which labeled particle volume as the feature to identify the trajectory of each particle during the triaxial compression tests. Alshibli et al. [19,20] focused on more sand particle properties, including volume, surface area, and dimension, which are incorporated into the particle-tracking method. Results showed that the particle kinematics and micro shear bands developed prior to the formation of persistent shear bands. More recent works have considered the local deformation gradient to examine the local shear component of displacement fields by using micro-strain [21] and translation gradient [22,23].

The digital image correlation (DIC) method has emerged as a promising method to elucidate full-field displacement fields that can provide a spatio-temporal continual description of sand deformation. This is based on pixel analysis of images taken during a specimen compression test, from which local displacements are evaluated by comparison of overlapping subsets of images captured at different deformation stages of the test. The effectiveness of DIC in the study of geomechanics has been demonstrated by many previous studies [17,24,25]. In particular, in shear band analysis, Rechenmacher and coworkers [26,27] used DIC to quantify the persistent shear bands and kinematic properties comprised of rotational and volumetric behaviors, as well as vortex structures of sand specimen undergoing plane strain deformation [28]. However, these works were carried out under two-dimensional stress conditions, which disregard the out-of-plane translational or rotational behaviors of the sand.

To elicit the 3D displacement field, a stereovision-based system of DIC analysis, namely, 3D-DIC, has been proposed and used in the characterization of material response [29,30]. However, no three-dimensional local strain or kinematics (translation, rotation, expansion/compaction, etc.) were revealed under triaxial compression conditions. This was due to the basic characteristic of DIC as an approach that performs non-intrusive sampling (i.e., boundary measurements only), thus, the specimen's internal deformation gradient, which is necessary for quantifying the motions of a 3D object, is consequently challenging to assess. Moreover, the selection of an appropriate coordinate system is another challenge. Ideally, the chosen coordinate system should align with the geometry of the studied object, so that deformation can faithfully represent how strain changed the object's geometry. Since the triaxial sand specimen is usually constituted in a cylindrical shape, the 3D cylindrical coordinate system is assumed suitable

for the characterization of micro- and meso-scale kinematics observed on the boundary of a deforming sand specimen under triaxial loading conditions.

In this paper, we provide the complete set of first-order 3D kinematic operators under cylindrical coordinates that are consistent with specimen geometry, and suitable to characterize micro- and meso-scale kinematics comprised of compressional, extensional, rotational, and shearing behaviors, for a series of sand triaxial compression tests. In Section 2, we give a brief introduction regarding the laboratory tests completed and coupled with the 3D DIC technique. In Section 3, we introduce 3D kinematic operators under cylindrical coordinates, as well as the use of these to characterize the local deformations. In Section 4, we provide the experimental design of kinematic analyses and the corresponding results. Section 5 presents the paper's findings and analyses of local kinematic phenomena observed and quantified on a series of sand specimens subjected to triaxial loading conditions. All supporting data and models needed to reproduce this paper are available at https://dataverse.tdl.org/dataverse/SGL, accessed on 1 August 2022.

2. Experimental Method

2.1. Triaxial Compression Test

Specimens constituted by dry sand, classified as SP, were tested under three-dimensional stress conditions [1]. The coefficients of uniformity and curvature were 2.34 and 1.11, respectively, providing the specimens an adequate range when viewed in grayscale; thus, the varying color patterns manifested on the specimen membrane can be distinguished through imaging correlation analysis. A subset from the experimental database of five tests was selected to for kinematic analysis. Basic physical properties and sample preparation methods of these tests are summarized in Table 1. All specimens from this subset were constituted approximately 160 mm in height and 70 mm in diameter. Three specimens had a relative density of more than 90.00% (092903b, 121304d, 121304c), one loose specimen had a relative density of 46.39% (121304b), and one two-layer specimen was constituted as bottom half "dense" (relative density of 98.97%) and top half "loose" (relative density of 30.54%) (120704c) [1]. The distinct density distribution produced by the two-layer specimen was intended for investigation of the effect of induced heterogeneity on the constitutive behavior of specimens (Table 1).

Table 1. Summary of sample characteristics.

Test Name	Height (mm)	Diameter (mm)	Relative Density (%)	Friction Angle (deg)	Peak (σ'_1/σ'_3)	Sample Preparation Method	Notes
092903b	155.50	71.33	91.09	49.51	7.35	Vibratory compaction	40 kPa confinement
121304d	159.50	71.38	99.71	50.95	7.95	Dry pluviation	20 kPa confinement
121304c	160.00	70.48	93.72	48.59	7.00	Dry pluviation	60 kPa confinement
121304b	158.17	70.86	46.39	40.88	4.79	Dry pluviation	Loose specimen (40 kPa)
120704c	157.67	70.88	68.90	43.71	5.43	Dry pluviation	Two-layer specimen (40 kPa)
	79.50	71.27	98.87	-	-		Lower part of two-layer specimen: dense sand
	78.17	70.68	30.54	-	-		Upper part of two-layer specimen: loose sand

A conventional triaxial apparatus performed the compression tests, except that the Plexiglass cell was removed to better capture the specimen's boundary displacement fields; thus, all specimens were vacuum consolidated. Three tests were consolidated to 40 kPa isotropic confining pressure (092903b, 121304c, and 120704c), and two tests were consolidated at confining pressures of 20 kPa (121304d) and 60 kPa (121304c), respectively. Axial loading compression was applied at a controlled axial strain rate of 0.2%/min until the specimen was fully sheared. Global axial stress–strain and strain–volumetric strain responses are shown in Figure 1. Note that due to the removal of the confining cell, the direct measurement of volumetric strain was not possible using the triaxial device; an

alternative methodology was therefore implemented to estimate the sample volume at every deformation stage through the reconstruction of the sample geometry using the stereo-digital images and the DIC to produce the material displacement field, and from there to estimate the volumetric strain. A detailed description of the methodology developed to assess the volumetric strain can be found in [25,31].

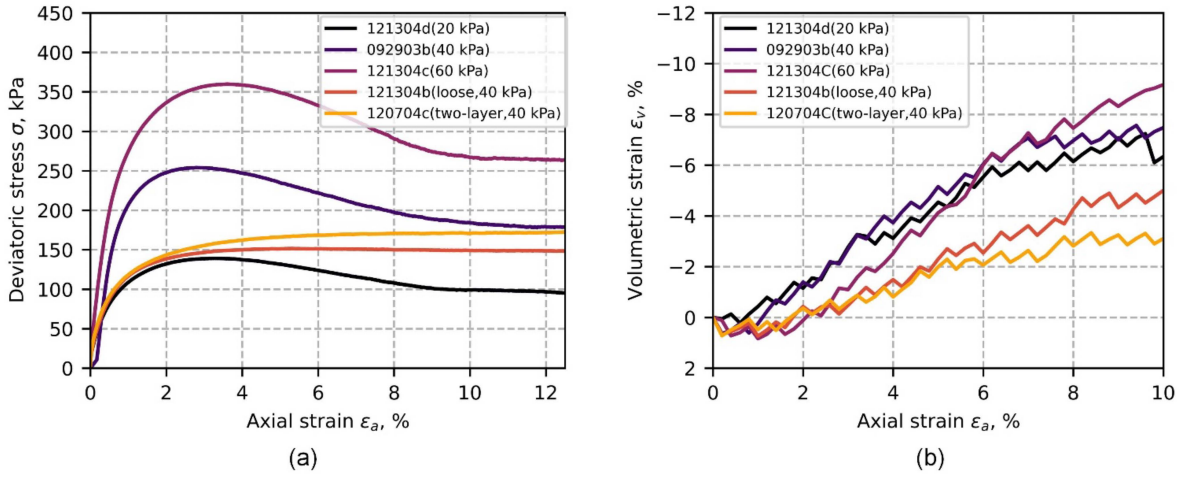

Figure 1. Global material responses: (**a**) triaxial stress-strain curves; (**b**) axial strain-volumetric strain curves.

Figure 1a shows peak stress occurred for dense specimens (tests 092903b, 121304d and 121304c), but not for loose and two-layer specimens (121304b and 120704c respectively). Comparison of constitutive behaviors of three dense specimens showed the peak stress increase with higher confinement. Figure 1b shows the volumetric strain behaviors of all tests, in which the dilation was seen among dense specimens, but was less significant for loose and two-layer specimens. Notice that the loose and two-layer specimens had similar volumetric behavior from the initial state up to 5% of axial strain, indicating that volumetric strain in the two-layer specimen was initially concentrated on its loose segment, which made it behave similarly to that of the loose specimen.

2.2. 3D Digital Image Correlation

The digital image correlation (DIC) method is a non-destructive, optical method for measuring displacement fields over the surface of a deforming body. The object tracked by DIC analysis is a cluster of image pixels forming a subset. When studying material evolved from initial state to deformed state, DIC measures the affine behaviors (i.e., translation, rotation, and/or straining) of overlapping subsets between the reference and target images. Due to the innate heterogeneity of sand colors, the distinct greyscale patterns of each subset can be directly recognized through a matching algorithm without any manual intervention. In this work, two digital cameras were obliquely set up in front of the specimen to construct a 3D scene, which is similar to the way human eyes acquire the object position [1]. The calibration of lenses involves capture-synchronous images of a standard grid oriented at different angles. From the resulting stereo images, key camera parameters (e.g., position, orientations, focal length, lenses distortions, etc.) are calibrated. After confirming the object's 3D spatial information, 3D displacements can be computed by comparing overlapping pixel subsets between reference and target images as described above.

The software VIC-3D, by Correlated Solutions, Inc. (Correlated Solutions: Irmo, SC, USA), was used to extract 3D displacement fields from the stereo images. The search for best-match subsets was implemented following normalized cross-correlation algorithm [32]. Once matching subsets and corresponding displacement vectors were identified, a continuous displacement field was linearly interpolated to evaluate subset translation, rotational, and straining properties on a continuum domain. Details of the piece-wise integration of cumulative displacement fields can be found in [25]. The stereo images were

taken every 15 s, corresponding to 0.05% of axial strain through the course of compression. An increment of 0.2% of axial strain, however, was considered sufficient to represent the evolution of localization effects [25,27]; thus, incremental displacements were updated every 4 images. The measurement accuracy was assessed by comparing averaged vertical displacement through DIC data with global readings by linear variable differential transformer (LVDT) transducers, and the difference was found approximately along the vertical direction. Similar accuracy has been observed in the horizontal direction [1,33].

To illustrate the components of a typical displacement field over the specimen's surface, Figure 2 presents displacement fields of test 092903b between axial strain 3.2% and 7.0% using the Lagrangian description resulting from 3D DIC analysis. The first row shows displacement vectors decomposed into horizontal (u), vertical (v), and out-of-plane (w) directions, respectively, based on a Euclidean coordinate system. The horizontal displacement, as anticipated, related to the development of an expansion band, which was concentrated in the middle of the specimen and made the sand move towards opposite directions (left negative, right positive) if viewed on the horizontal plane. The vertical displacement field (middle sub-plot in the same row) showed approximately zero displacement at the top (since loading was provided from the bottom) suggesting that the specimen was compressed approximately as three separate "moving blocks" that possessed different deforming rates [29]. The bulging effect of the specimen is depicted in the plot of the out-of-plane displacement field (third sub-plot), in which the maximum value was shown at the center of specimen. The second row in Figure 2 is the same displacement vector, but decomposed under cylindrical coordinates, yielding radial (r), tangential (t), and vertical (v) displacement fields, respectively (left to right). Amidst the three, the tangential displacement (middle sub-plot in the same row) shows an intensified region along the diagonal direction, suggesting local areas tended to rotate clockwise along the specimen circumference. This agrees well with previous findings on the intense rolling of particles within the shear band [12,34].

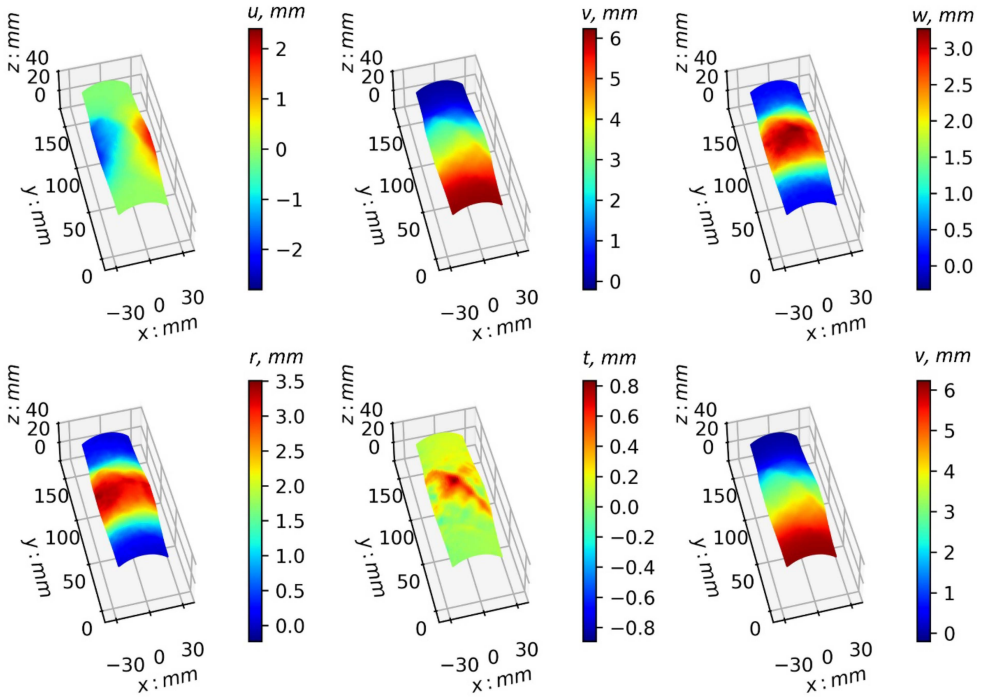

Figure 2. First row is displacement fields of test 092903b between axial strain 3.2% and 7.0%; left to right are displacements along horizontal (u), vertical (v), and out-of-plane (w) directions based on a spatial coordinate system. Second row is the same displacement field, but decomposed into radial (r), tangential (t), and vertical (v) directions on cylindrical coordinates.

3. 3D Kinematic Operators under Cylindrical Coordinates

This paper focuses on linking the localization effects with kinematic effects as observed on the boundary of the specimen, such as compression, rotation, and/or straining, which may lead to specific mechanistic failure mechanisms. A cylindrical coordinate system was considered as the basis to maintain consistency with specimen geometry, and thought to be suitable for presenting the state of three-dimensional stresses. The observed displacement fields across the specimen boundary were decomposed in radial, tangential, and vertical directions. One challenge in calculating kinematics under current setting lies in the difficulty of computing directional derivatives along radial directions, since no contiguous measurements of internal deformations are retrieved by the DIC sampling method (i.e., DIC only measures boundary displacement fields). To overcome this issue, we introduced a series of auxiliary assumptions; namely, a set of reference origins along the axis of the specimen where the radial and tangential displacements were assumed to be zero; and the displacements along the axis were estimated to be equal to the average of all vertical displacements captured on the specimen boundary at each specimen height. This assumption was supported by experimental evidence revealed by Desrues et al. [35]—a rigid cone delimited by a circular shear surface and multiple sets of planes extending outwards from the cone towards the specimen boundary imply that the radial and tangential displacements along the axis are negligible compared to vertical displacement. Figure 3 illustrates this assumption, in which the sampling area from a spatial surface is transformed into a series of 3D wedges by incorporating this set of auxiliary reference origins; thus, the localization effects can be properly evaluated from the kinematics of these 3D shapes.

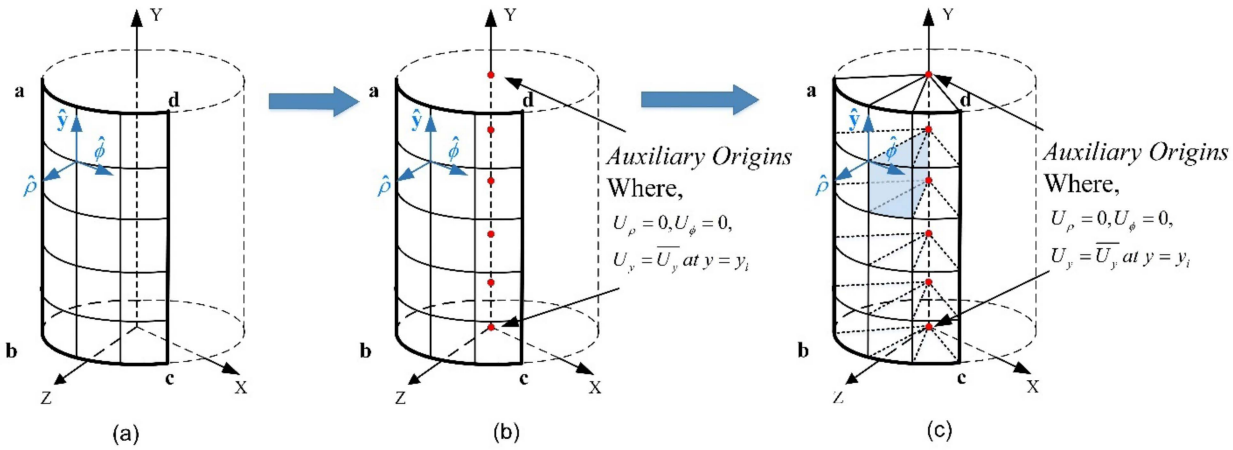

Figure 3. Schematic illustration of 3D study objects: (**a**) the initial geometry of the specimen; (**b**) the assumed auxiliary origins along the axis of the specimen; (**c**) connecting boundary coordinates with added auxiliary origins to form the 3D study objects.

After discretizing the continuum media as described above, it follows to identify the kinematic operators under the current configuration. The conventional first-order kinematics include *gradient*, *divergence*, and *curl* operators acting on the vector field U [36]. These quantities are defined through an operator called *del*, or *nabla*, and its tensor, dot, and cross product with the vector field U. Equations (1)–(3) provide the expressions of *gradient*, *divergence*, and *curl* under cylindrical coordinates. The *gradient* of a 3D vector field U would generate a *deformation tensor* F, composed of nine components representing translational or rotational changing rates of the neighboring local area affected by the vector field U. The sum of diagonal terms presented in F is the *divergence* indicating the total magnitude of sink (positive quantities) or source (negative quantities) of a local area. Moreover, the difference between every two off-diagonal terms in F gives each component of *curl* representing

local rotational behavior with respect to every axis. Full derivation of first-order kinematic operators under the cylindrical coordinates can be found in Appendix A.

$$grad\ U = \nabla \otimes U = \begin{bmatrix} F_{11} & F_{12} & F_{13} \\ F_{21} & F_{22} & F_{23} \\ F_{31} & F_{32} & F_{33} \end{bmatrix} = \begin{bmatrix} \frac{\partial U_\rho}{\partial \rho} & \frac{1}{\rho}\left(\frac{\partial U_\rho}{\partial \phi} - U_\phi\right) & \frac{\partial U_\rho}{\partial y} \\ \frac{\partial U_\phi}{\partial \rho} & \frac{1}{\rho}\left(\frac{\partial U_\phi}{\partial \phi} + U_\rho\right) & \frac{\partial U_\phi}{\partial y} \\ \frac{\partial U_y}{\partial \rho} & \frac{1}{\rho}\frac{\partial U_y}{\partial \phi} & \frac{\partial U_z}{\partial y} \end{bmatrix} \quad (1)$$

$$div\ U = \nabla \cdot U = \frac{1}{\rho}\frac{\partial}{\partial \rho}(U_\rho \cdot \rho) + \frac{1}{\rho}\frac{\partial U_\phi}{\partial \phi} + \frac{\partial U_y}{\partial y} \quad (2)$$

$$\begin{aligned} curl\ U = \nabla \times U &= (curl\ U)_\rho + (curl\ U)_\phi + (curl\ U)_y \\ &= \left(\frac{1}{\rho}\frac{\partial U_y}{\partial \phi} - \frac{\partial U_\phi}{\partial y}\right)\hat{\rho} + \left(\frac{\partial U_\rho}{\partial y} - \frac{\partial U_y}{\partial \rho}\right)\hat{\phi} \\ &+ \left(\frac{1}{\rho}\frac{\partial}{\partial \rho}(U_\phi \cdot \rho) - \frac{1}{\rho}\frac{\partial U_\rho}{\partial \phi}\right)\hat{y} \end{aligned} \quad (3)$$

Figure 4 provides an example of nine components of the *gradient* field (Equation (1)) based on the state of a specimen's boundary displacements (*092903b*), from undeformed stage to critical state (axial strain 0.0% to 9.6%). The x-y coordinates are normalized according to specimen diameter to enable comparison of the results with other tests. Expansional behavior presented in radial and tangential directions, as shown by positive values in F_{11} and F_{22}. Along the vertical direction, however, compression was observed inside the shearing zone, especially located at the top-left portion, as shown in F_{33}. The overall volumetric behavior in terms of these two competing phenomena can be found in the plot of the divergence field, as shown in Figure 5. A general volumetric dilation was seen in the middle of the specimen; in particular, a local concentrating zone was found to coincide with areas of shear band. Nevertheless, inside the compression band, which was characterized as negative *divergence*, intense volumetric contraction was found matching with areas of large axial compression, as shown in F_{33}. This revealed that the shear band can introduce highly volumetric expansion or compaction, depending on its overlap with the expansion band or compression band. This observation complements those from previous studies about volumetric change influenced by shear band, which focused on the large voids (volumetric dilation) generated by intense rolling of soil particles under the plane strain conditions [34,37].

Figure 6 presents the curl fields with respect to three orthogonal axes. Sub-plots (d), (e), and (f) illustrate the positive rotational directions for each axis. In Figure 6a, a shear band is explicitly depicted by highlighted clockwise rotational areas. This corroborates, again, intense rolling of soil particles occurring inside the shear band [34,37]. For rotation with respect to $\hat{\phi}$ axis (as shown in Figure 6b), two bands are seen rotating in opposite directions and separated by a neutral zone in the middle, suggesting the "barrel" shape of expansion band. As for curl along $\hat{y}$ axis, an approximate zero rotation is seen across the whole domain, except for some deviations found along the shear banding areas, suggesting that the variations in axisymmetric deformation of the specimen were introduced by the development of the shear band.

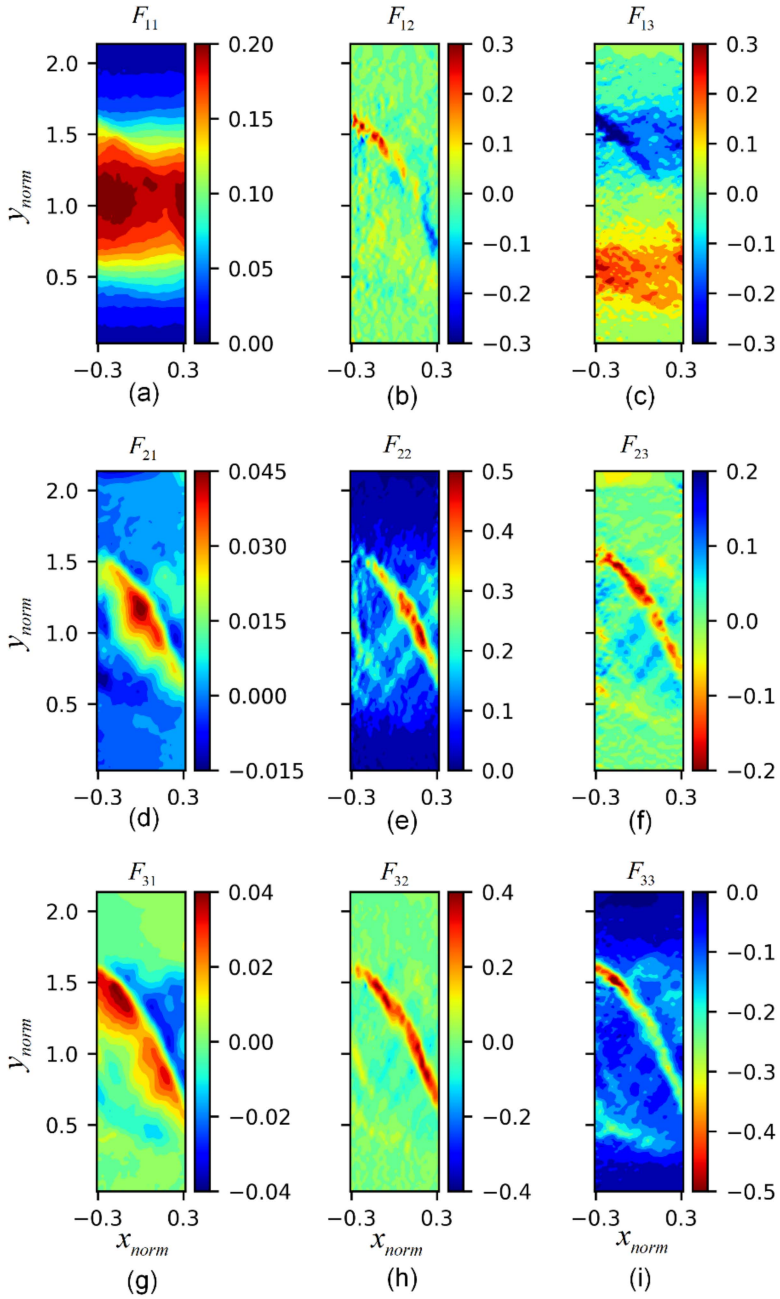

Figure 4. Nine components of gradient deformation tensor F based on test *092903b* from undeformed stage to loading level of $\varepsilon_a = 9.6\%$: (**a**) tenor component F_{11}; (**b**) tenor component F_{12}; (**c**) tenor component F_{13}; (**d**) tenor component F_{21}; (**e**) tenor component F_{22}; (**f**) tenor component F_{23}; (**g**) tenor component F_{31}; (**h**) tenor component F_{32}; (**i**) tenor component F_{33}.

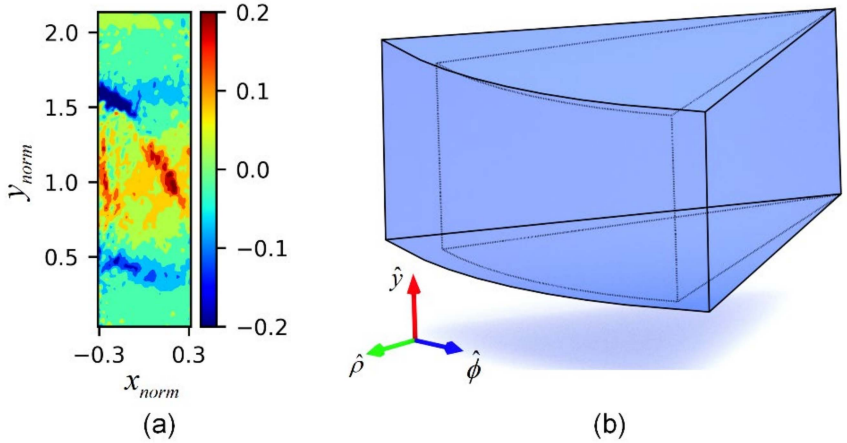

Figure 5. (**a**) *Divergence* field based on test *092903b* at loading level of $\varepsilon_a = 9.6\%$; (**b**) illustration of deformation associated with positive *divergence* field.

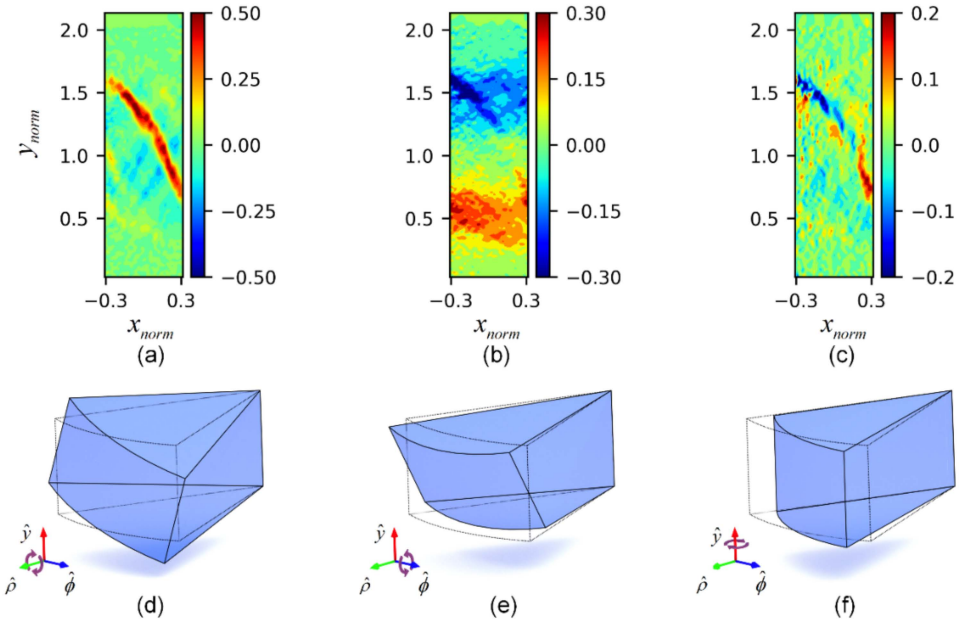

Figure 6. Curl components calculated based on test *092903b* at loading level of $\varepsilon_a = 9.6\%$: (**a**) curl field with respect to $\hat{\rho}$ axis; (**b**) curl field with respect to $\hat{\phi}$ axis; (**c**) curl field with respect to $\hat{y}$ axis; (**d**) illustration of positive rotation for curl along $\hat{\rho}$ axis; (**e**) illustration of positive rotation for curl along $\hat{\phi}$ axis; (**f**) illustration of positive rotation for curl along $\hat{y}$ axis.

4. Spatio-Temporal Evolution of 3D Kinematics

4.1. Experimental Design

To investigate the evolution of localization effects in space and time, an experimental design was formulated to account for tests showing distinct experimental conditions. Figure 7 shows the accumulated strain windows for the analysis; specifically, axial strains from 0.0% to 1.0%, 1.0% to 3.0%, 3.0% to 5.0%, 5.0% to 7.0%, and 7.0% to 9.0%, respectively. The first two windows, 0.0%–1.0% and 1.0%–3.0%, correspond to the elastic and hardening phases for most of the tests. After peak stress around 3.0% axial strain, dense specimens entered the softening stage, while no clear softening was presented in the loose and layered specimens. Figure 8 illustrates the experimental design of the proposed kinematic analysis. Four kinematic features, *gradient* along $\hat{\rho}$ axis (F_{11}), *gradient* along $\hat{y}$ axis (F_{33}), *divergence* (*div U*), and *curl* along $\hat{\rho}$ axis ($(curl\ U)_\rho$), were investigated across all tests. The associated deformation characteristics were: F_{11} indicates radial deformation gradient; F_{33}

indicates vertical deformation gradient; $div\,U$ indicates volumetric deformation gradient; and $(curl\,U)_\rho$ indicates rotational deformation gradient. The criteria for choosing these kinematic signatures lay in the significant rotational or volumetric behavior associated with the development of compaction, expansion, and shear bands. For each strain window, the kinematic quantities were tracked on the reference to the initial image of that window; thus, the results were computed on the Lagrangian description.

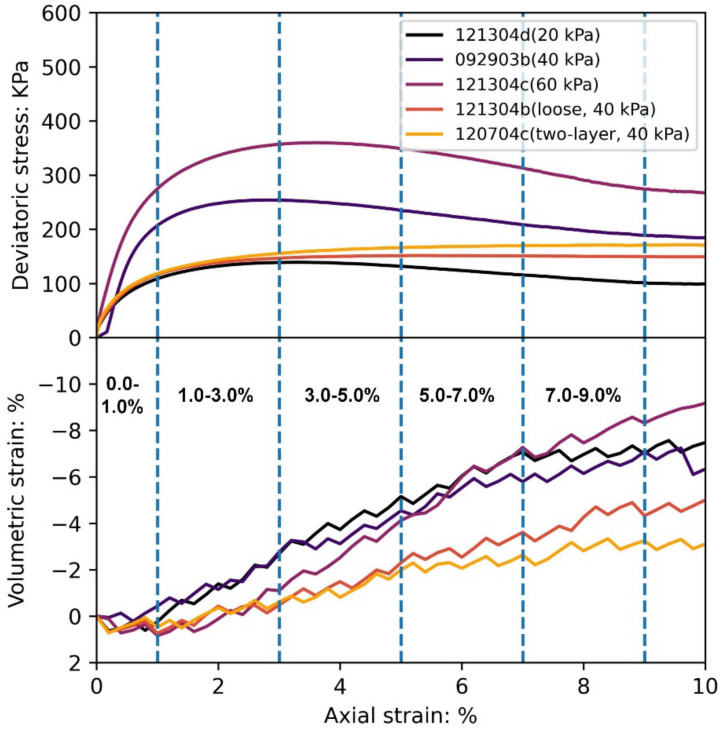

Figure 7. Strain windows for kinematic analyses: 0.0–1.0%, 1.0–3.0%, 3.0–5.0%, 5.0–7.0%, and 7.0–9.0% of axial strain.

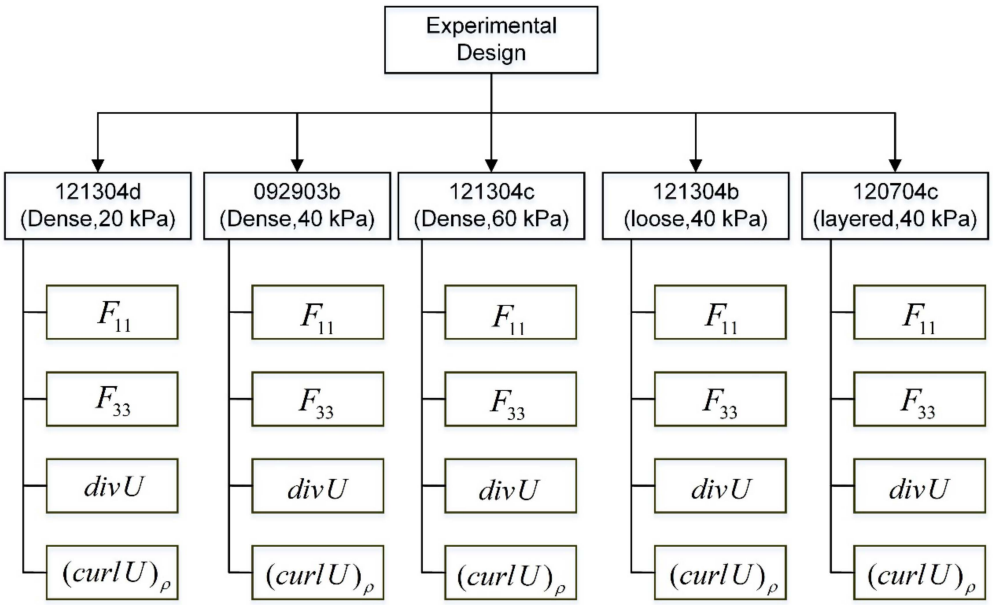

Figure 8. Experimental design of analyzing kinematic properties divergence; *gradient* along $\hat{\rho}$ axis (F_{11}), *gradient* along $\hat{y}$ axis (F_{33}), *divergence* ($div\,U$), and *curl* along $\hat{\rho}$ axis ($(curl\,U)_\rho$).

4.2. Dense specimen at Confinement of 40 kPa (Test 092903b)

Figure 9 presents the five increments of the divergence field of test 092903b. Results reveal that local dilation started as early as the hardening phase (axial strain 1.0%–3.0%), and its further development introduced compression bands appearing in the adjacent areas of the expansion band. The plot of the curl along $\hat{\rho}$ axis in Figure 10 shows that surface rotation localized after the peak stress (i.e., after second frame). When the persistent shear band was fully formed, the surrounding areas tended to rotate along opposite directions, in contrast to that of the inside the shear band. The gradient along the radial direction F_{11} (Figure 11) indicates the expansion band, which started from the hardening stage. It distributed uniformly around the middle portion of the specimen until the occurrence of the dominant shear band, which broke the symmetry with respect to the middle of the specimen. Additionally, the magnitude of expansion decreased in the last frame, suggesting that dilation declined when loading approached the critical state. Figure 12 presents the evolution of local vertical deformation F_{33}. The shear band is highlighted by this property, indicating the local compression was evident inside the shear band, which may have been caused by the forms and collapses of force chains within the banding area [12].

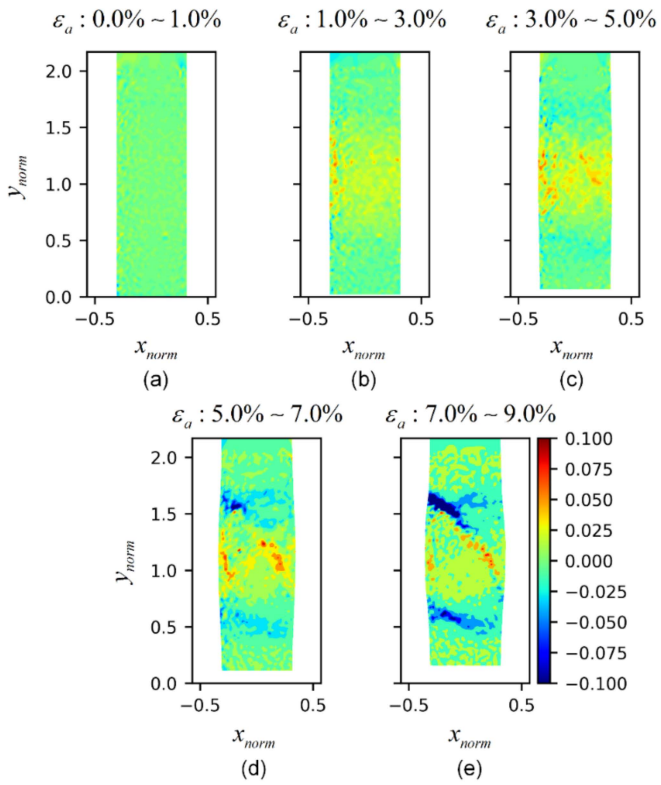

Figure 9. Evolution of *divergence* fields *div U* of test 092903b: (**a**) axial strain 0.0%–1.0%; (**b**) axial strain 1.0%–3.0%; (**c**) axial strain 3.0%–5.0%; (**d**) axial strain 5.0%–7.0%; (**e**) axial strain 7.0%–9.0%.

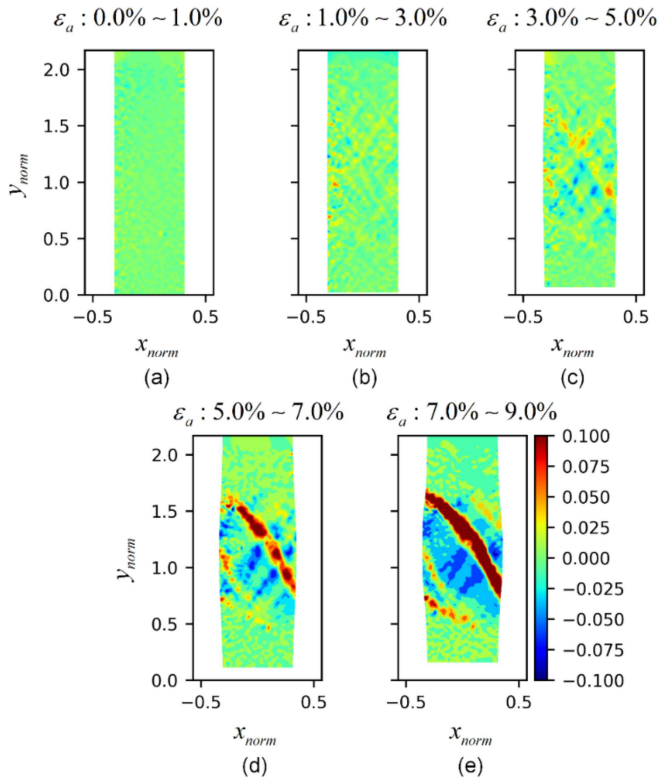

Figure 10. Evolution of *curl* along $\hat{\rho}$ axis $(curl\ U)_\rho$ of test 092903b: (**a**) axial strain 0.0%–1.0%; (**b**) axial strain 1.0%–3.0%; (**c**) axial strain 3.0%–5.0%; (**d**) axial strain 5.0%–7.0%; (**e**) axial strain 7.0%–9.0%.

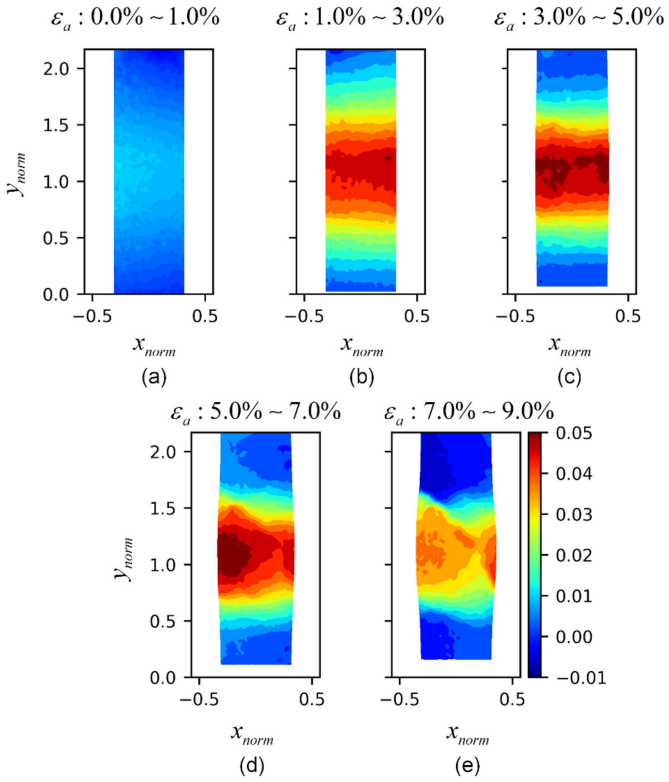

Figure 11. Evolution of gradient along $\hat{\rho}$ axis F_{11} of test 092903b: (**a**) axial strain 0.0%–1.0%; (**b**) axial strain 1.0%–3.0%; (**c**) axial strain 3.0%–5.0%; (**d**) axial strain 5.0%–7.0%; (**e**) axial strain 7.0%–9.0%.

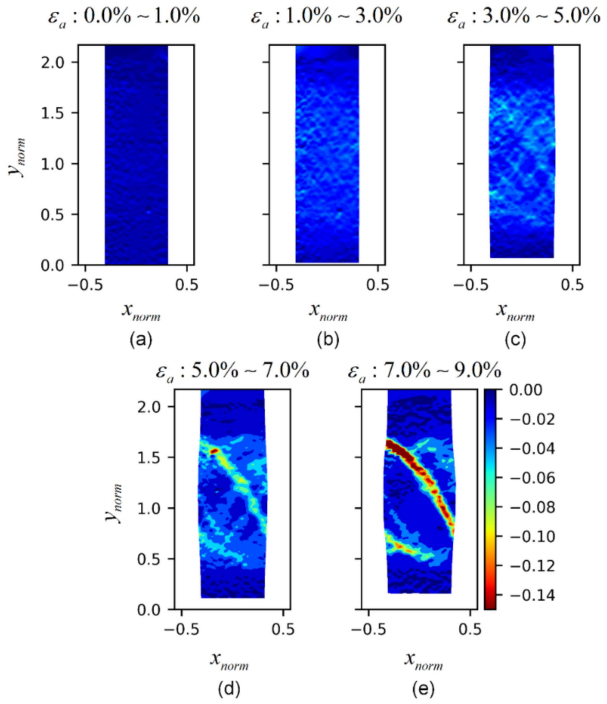

Figure 12. Evolution of gradient along $\hat{y}$ axis F_{33} of test 092903b: (**a**) axial strain 0.0%–1.0%; (**b**) axial strain 1.0%–3.0%; (**c**) axial strain 3.0%–5.0%; (**d**) axial strain 5.0%–7.0%; (**e**) axial strain 7.0%–9.0%.

4.3. Dense Specimen at Confinement of 20 kPa (Test 121304d)

Figures 13 and 14 describe the progression of *divergence* and *curl* along $\hat{\rho}$ axis of a dense specimen under relatively low confinement 20 kPa. Both figures indicate that the shear band only developed at a very late stage (axial strain 7.0%–9.0%). This agrees well with the findings in Liu et al. [38] that localization increases with higher confining pressures under the plane strain condition. The plot of *gradient* along $\hat{\rho}$ axis F_{11} (Figure 15) shows that the middle expansion started from an axial strain of 1.0%–3.0%. Later, with the development of shear band, the expanding zone was bounded, and leading the radial deformation was only active within the shear band. The plot of gradient along $\hat{y}$ axis F_{33} (Figure 16) suggests the shear band was not fully formed until the last frame. After a persistent shear band dominated the shear process, the intense local axial deformation was only apparent within the banding area.

4.4. Dense Specimen at Confining Pressure 60 kPa (Test 121304c)

This dense specimen was performed under a higher confinement compared to the other tests. Figure 17 shows the progress of divergence field based on the dense specimen under confining pressure of 60 kPa. The local volumetric expansion was seen to occur immediately after the peak stress (axial strain 3.0%). The compacting region later emerged in the upper and lower area of expansion band (strain window 3.0%–5.0%), but only one at the top persisted to the end of the softening stage. Figure 18 shows under this experimental condition at least three shear bands progressing simultaneously with different shapes and orientations. The radial deformation gradient for this specimen, as presented in Figure 19, developed uniformly along the horizontal direction until the achievement of 7.0% axial strain. When the shearing reached the critical state (strain window 3.0%–5.0%), the intense radial deformation was seen encompassed within a "butterfly" zone (Figure 19e), which was due to two shear bands that developed along cross-diagonal directions at this stage of loading (Figure 18e). Figure 20 shows that deformation along the vertical direction were localized in all three persistent shear bands once they were fully formed. In sum, the findings in the dense specimen under high confinement suggests a stronger localization pattern compared to that of the lower-density confined specimen in the triaxial compression test.

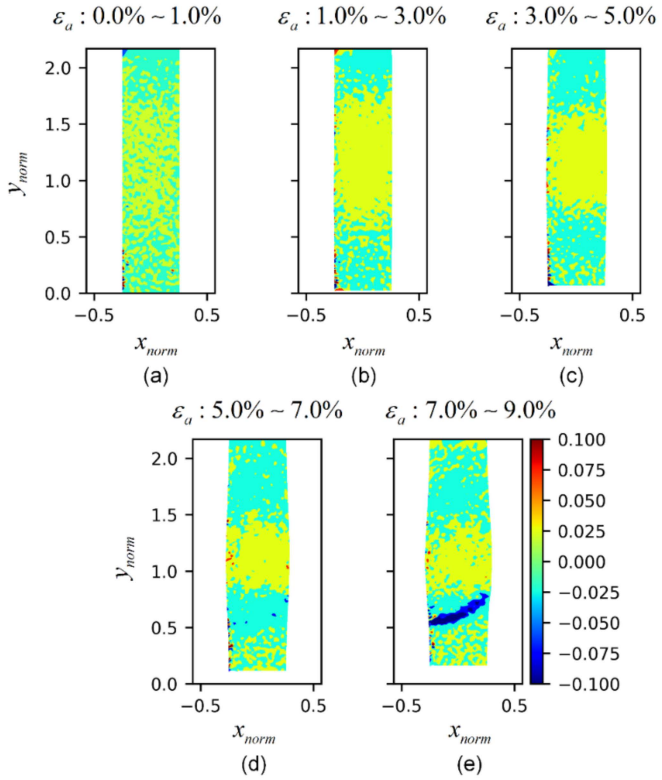

Figure 13. Evolution of *divergence* field *div U* of test 121304d: (**a**) axial strain 0.0%–1.0%; (**b**) axial strain 1.0%–3.0%; (**c**) axial strain 3.0%–5.0%; (**d**) axial strain 5.0%–7.0%; (**e**) axial strain 7.0%–9.0%.

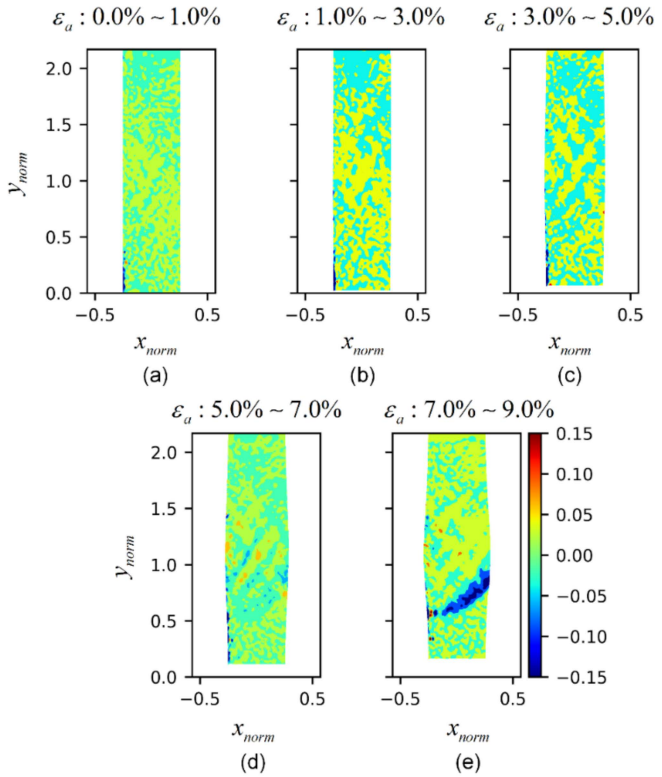

Figure 14. Evolution of *curl* along $\hat{\rho}$ axis $(curl\ U)_\rho$ of test 121304d: (**a**) axial strain 0.0%–1.0%; (**b**) axial strain 1.0%–3.0%; (**c**) axial strain 3.0%–5.0%; (**d**) axial strain 5.0%–7.0%; (**e**) axial strain 7.0%–9.0%.

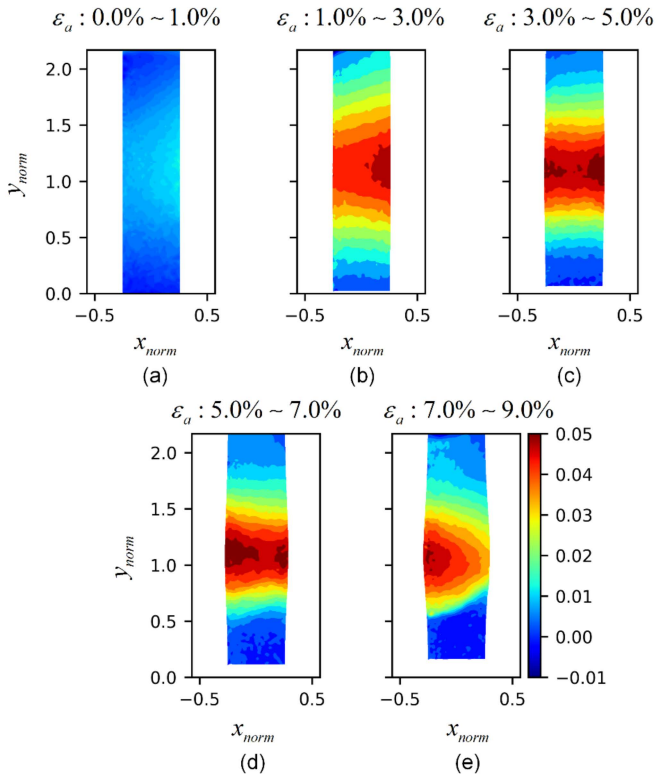

Figure 15. Evolution of *gradient* along $\hat{\rho}$ axis F_{11} of test 121304d: (**a**) axial strain 0.0%–1.0%; (**b**) axial strain 1.0%–3.0%; (**c**) axial strain 3.0%–5.0%; (**d**) axial strain 5.0%–7.0%; (**e**) axial strain 7.0%–9.0%.

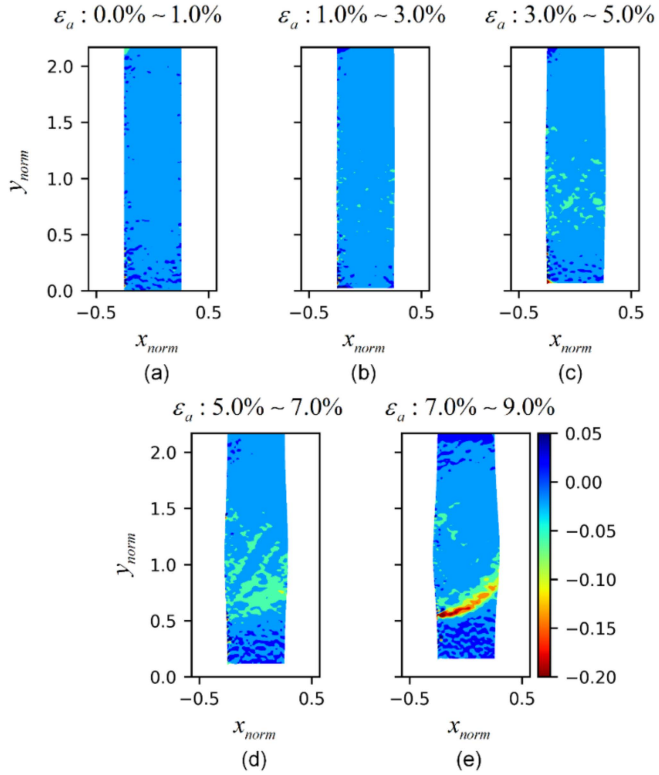

Figure 16. Evolution of *gradient* along $\hat{y}$ axis F_{33} of test 121304d: (**a**) axial strain 0.0%–1.0%; (**b**) axial strain 1.0%–3.0%; (**c**) axial strain 3.0%–5.0%; (**d**) axial strain 5.0%–7.0%; (**e**) axial strain 7.0%–9.0%.

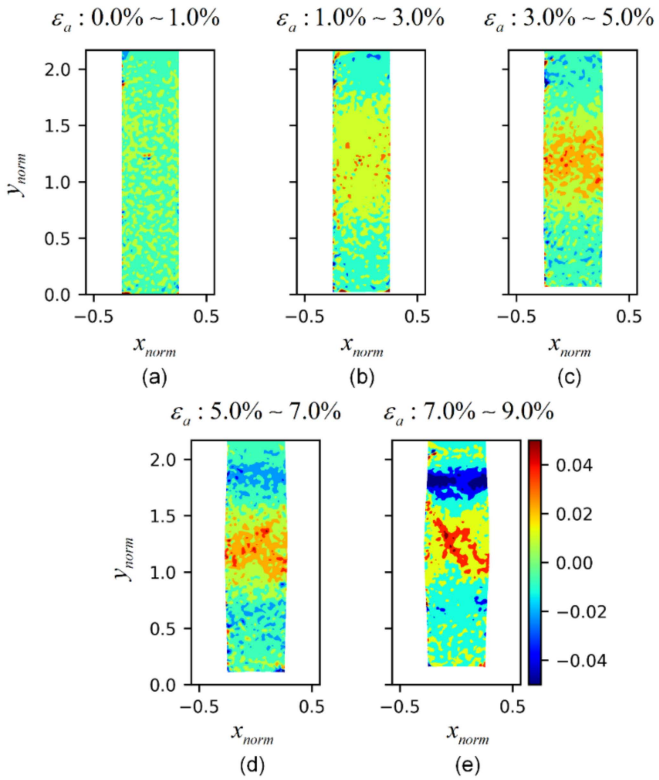

Figure 17. Evolution of *divergence* field *div U* of test 121304c: (**a**) axial strain 0.0%–1.0%; (**b**) axial strain 1.0%–3.0%; (**c**) axial strain 3.0%–5.0%; (**d**) axial strain 5.0%–7.0%; (**e**) axial strain 7.0%–9.0%.

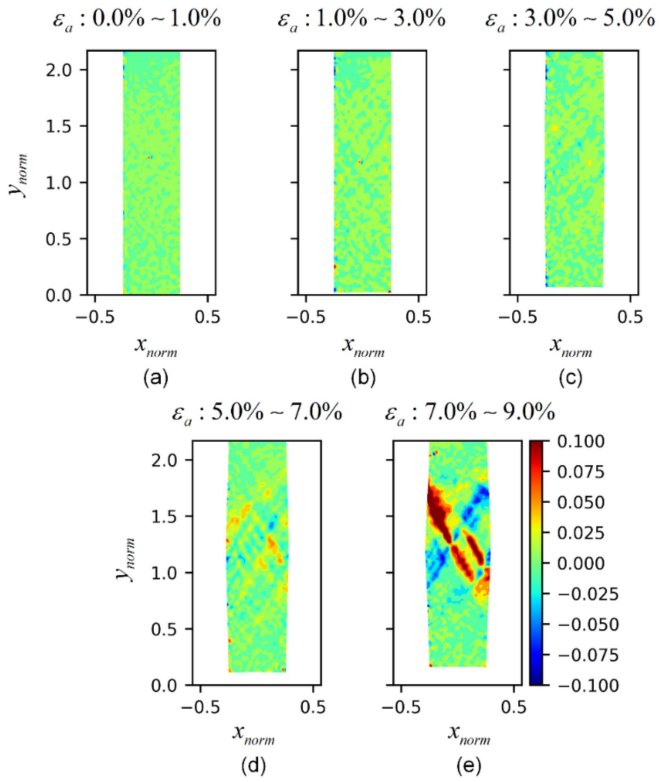

Figure 18. Evolution of *curl* along $\hat{\rho}$ axis $(curl\ U)_\rho$ of test 121304c: (**a**) axial strain 0.0%–1.0%; (**b**) axial strain 1.0%–3.0%; (**c**) axial strain 3.0%–5.0%; (**d**) axial strain 5.0%–7.0%; (**e**) axial strain 7.0%–9.0%.

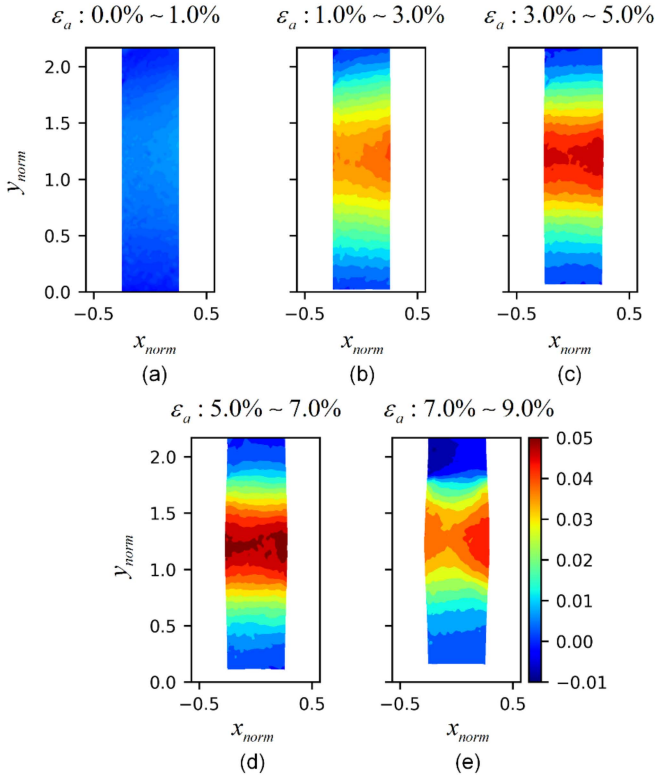

Figure 19. Evolution of *gradient* along $\hat{\rho}$ axis F_{11} of test 121304c: (**a**) axial strain 0.0%–1.0%; (**b**) axial strain 1.0%–3.0%; (**c**) axial strain 3.0%–5.0%; (**d**) axial strain 5.0%–7.0%; (**e**) axial strain 7.0%–9.0%.

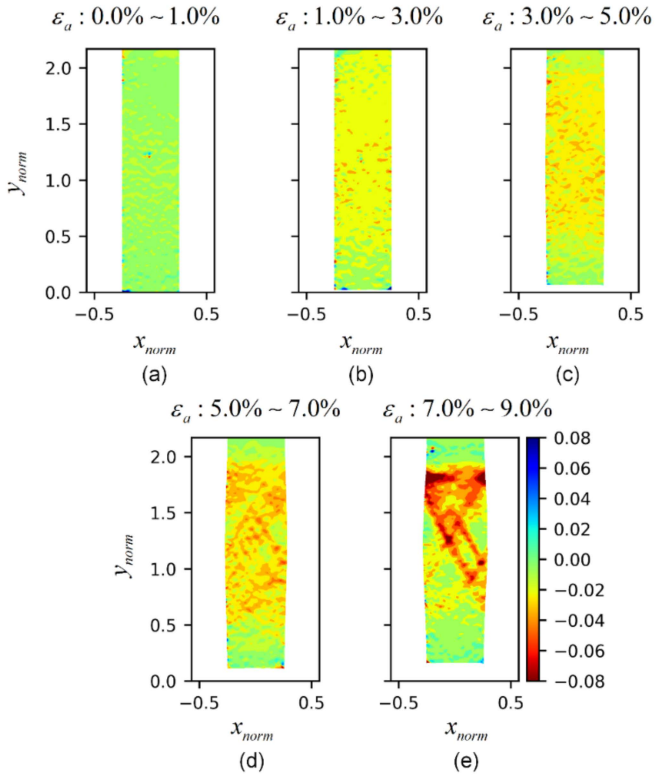

Figure 20. Evolution of *grad* along $\hat{y}$ axis F_{33} of test 121304c: (**a**) axial strain 0.0%–1.0%; (**b**) axial strain 1.0%–3.0%; (**c**) axial strain 3.0%–5.0%; (**d**) axial strain 5.0%–7.0%; (**e**) axial strain 7.0%–9.0%.

4.5. Loose Specimen at Confining Pressure 40 kPa (Test 121304b)

Figure 21 shows the local divergence development of the loose specimen during compression. Only a slight expansion appeared at the lower part of the specimen, suggesting volumetric dilation was much less evident for the loose specimen compared to the dense ones. This moderate change pattern was also found in shear band evolution. As presented in Figure 22, even though two seemingly shear bands were gradually formed along opposite directions, the pattern was not significant when loading approached axial strain of 9.0%. The slow development of localization effects is also implied by the plot of gradient along $\hat{\rho}$, as in Figure 23, which shows that the radius change followed a constant pattern after axial strain of 3.0%, and the interactions between expansion and shear bands are not apparent. Figure 24 shows the similar localization patterns as that of Figure 22.

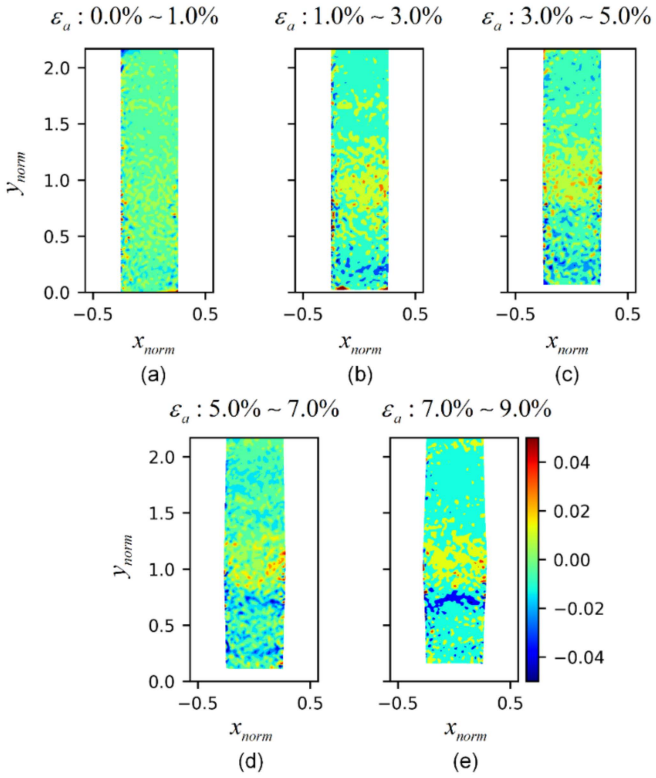

Figure 21. Evolution of divergence field *div U* of test 121304b: (**a**) axial strain 0.0%–1.0%; (**b**) axial strain 1.0%–3.0%; (**c**) axial strain 3.0%–5.0%; (**d**) axial strain 5.0%–7.0%; (**e**) axial strain 7.0%–9.0%.

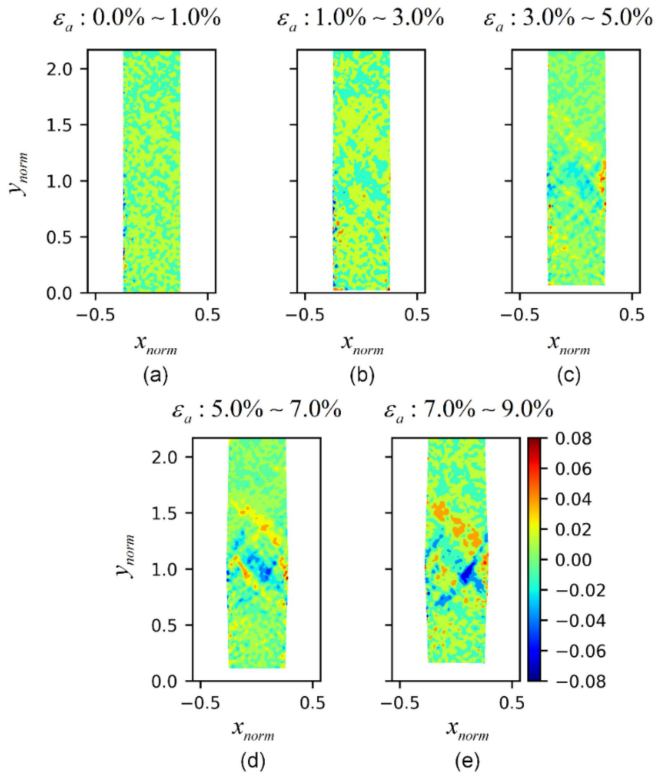

Figure 22. Evolution of curl along $\hat{\rho}$ axis $(curl\ U)_\rho$ of test 121304b: (**a**) axial strain 0.0%–1.0%; (**b**) axial strain 1.0%–3.0%; (**c**) axial strain 3.0%–5.0%; (**d**) axial strain 5.0%–7.0%; (**e**) axial strain 7.0%–9.0%.

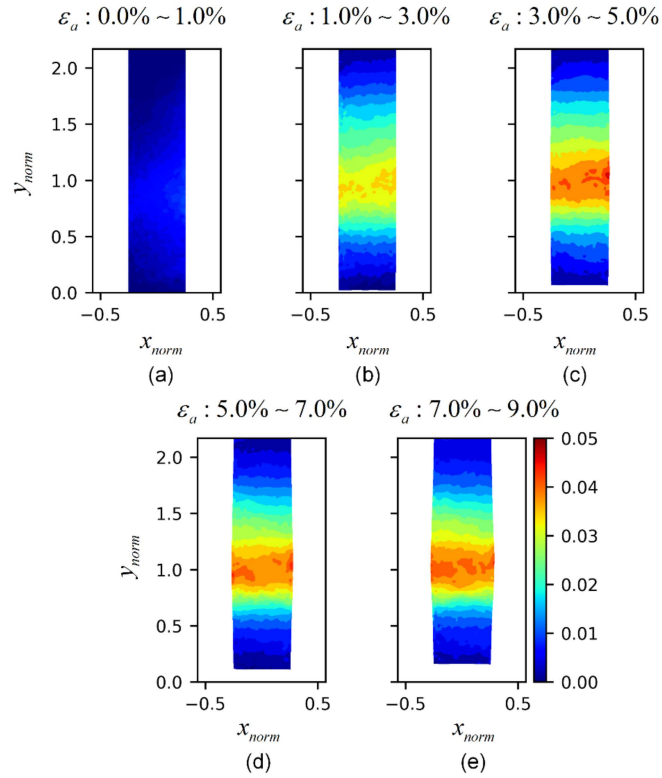

Figure 23. Evolution of gradient along $\hat{\rho}$ axis F_{11} of test 121304b: (**a**) axial strain 0.0%–1.0%; (**b**) axial strain 1.0%–3.0%;(**c**) axial strain 3.0%–5.0%;(**d**) axial strain 5.0%–7.0%;(**e**) axial strain 7.0%–9.0%.

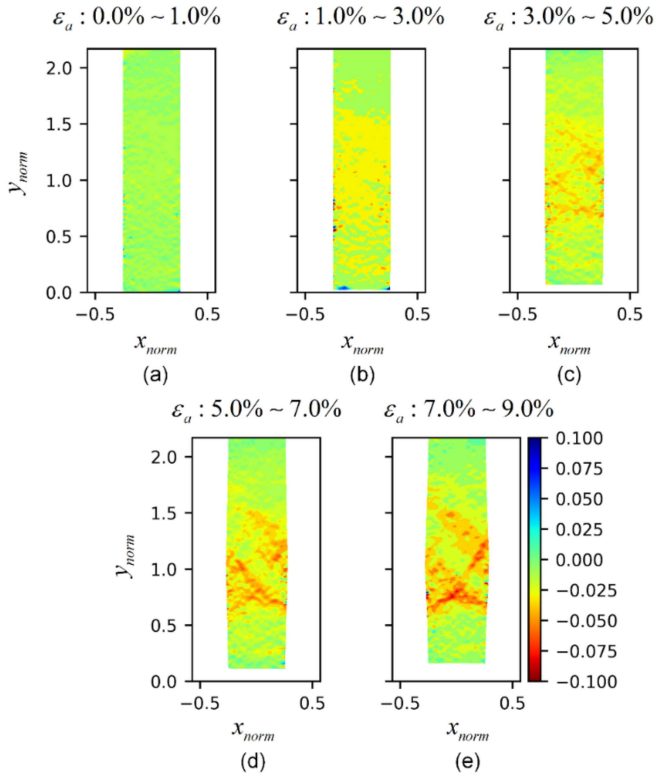

Figure 24. Evolution of gradient along $\hat{y}$ axis F_{33} of test 121304b: (**a**) axial strain 0.0%–1.0%; (**b**) axial strain 1.0%–3.0%; (**c**) axial strain 3.0%–5.0%; (**d**) axial strain 5.0%–7.0%; (**e**) axial strain 7.0%–9.0%.

4.6. Layered Specimen at Confining Pressure of 40 kPa (Test 120704c)

The image acquisition of the layered specimen (test 120704c) captured some 'extreme values' of kinematic properties occurring at the boundary of the imaging area. This can be interpreted in the stereo images, as shown in Figure 25, where the bumpy, complex, and heterogeneous deforming patterns are seen in the upper budging part of the specimen. One hypothesis is that it could be attributed to the distinctive material density constituting the upper and lower parts of the specimen (relative densities are 30.54% vs. 98.87%, as presented in Table 1). When the specimen was undergoing triaxial shearing, the local density changed significantly for both the upper and lower parts of the specimen, which encoded more heterogeneous deformation patterns in the local displacements. Figure 26 presents the evolution of divergence field of the specimen. Figure 27 shows no clear shear banding was developed over the image-capturing area, which was similar to that of the loose specimen. Figure 28 shows that the expansion mainly happened to the upper loose part, indicating the failure was governed by the weak part of the specimen. The results of the test on the layered specimen showed an overall similar behavior to that of the loose specimen, including localizations of expansion and shearing phenomena. Figure 29 shows the evolution of gradient along $\hat{y}$ axis F_{33} of test 120704c, in which the non-significant vertical strain localization observed among the majority of surface areas.

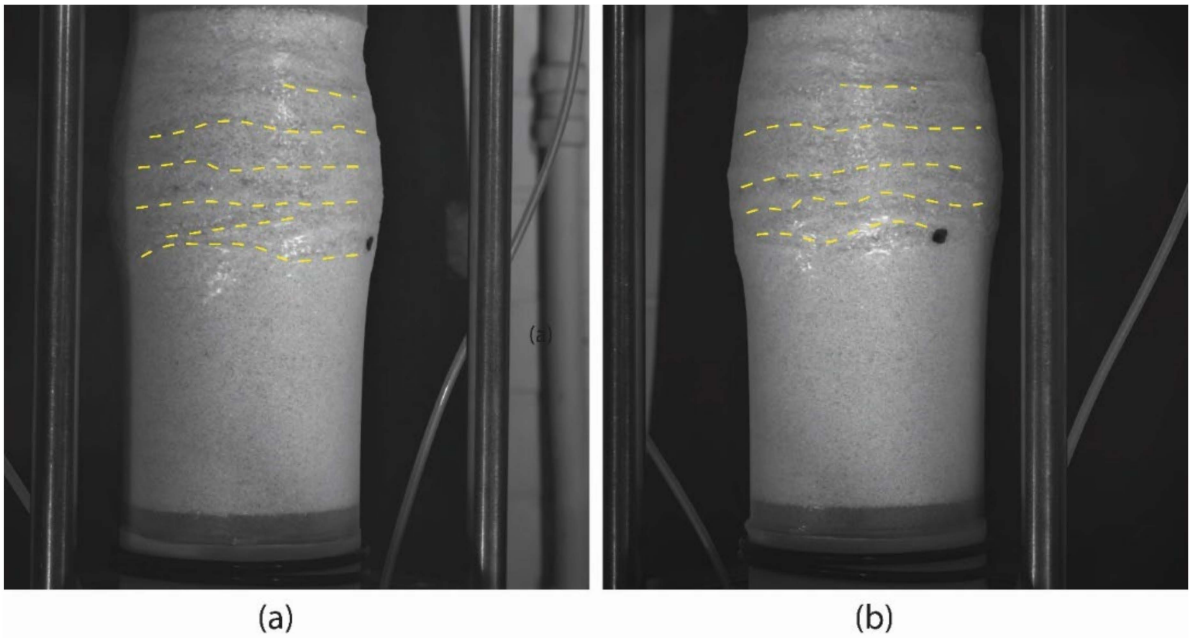

Figure 25. Digital images of test 120704c at axial strain 9.0%: (**a**) left image; (**b**) right image.

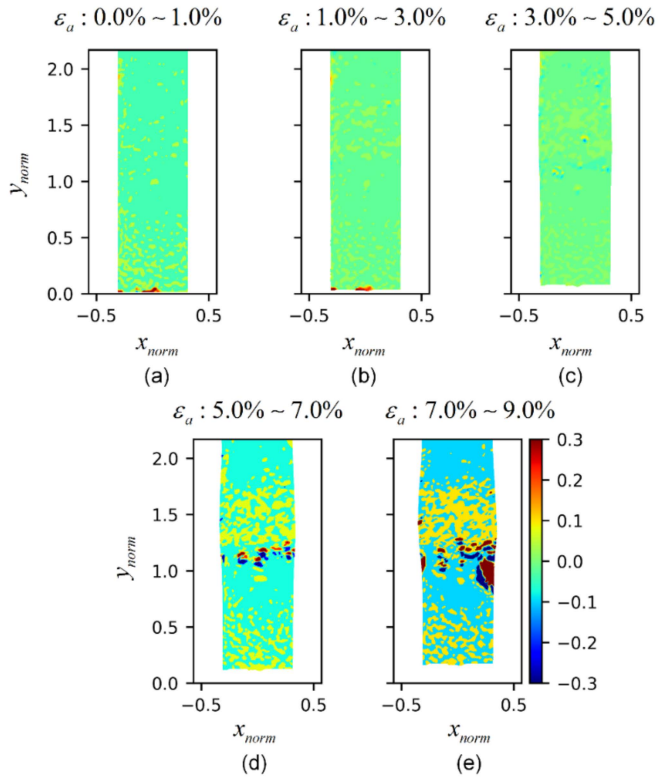

Figure 26. Evolution of divergence field *div U* of test 120704c: (**a**) axial strain 0.0%–1.0%; (**b**) axial strain 1.0%–3.0%; (**c**) axial strain 3.0%–5.0%; (**d**) axial strain 5.0%–7.0%; (**e**) axial strain 7.0%–9.0%.

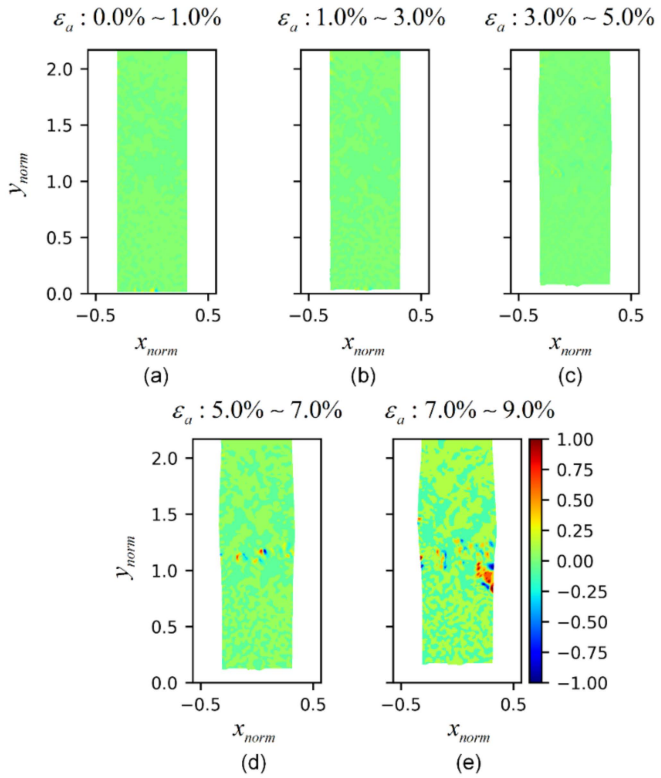

Figure 27. Evolution of curl along $\hat{\rho}$ axis $(curl\ U)_\rho$ of test 120704c: (**a**) axial strain 0.0%–1.0%; (**b**) axial strain 1.0%–3.0%; (**c**) axial strain 3.0%–5.0%; (**d**) axial strain 5.0%–7.0%; (**e**) axial strain 7.0%–9.0%.

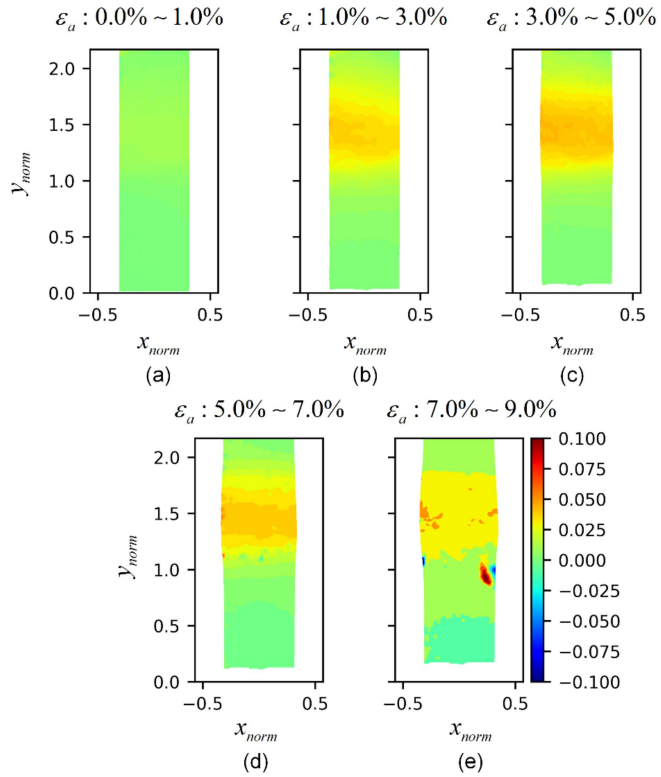

Figure 28. Evolution of gradient along $\hat{\rho}$ axis F_{11} of test 120704c: (**a**) axial strain 0.0%–1.0%; (**b**) axial strain 1.0%–3.0%; (**c**) axial strain 3.0%–5.0%; (**d**) axial strain 5.0%–7.0%; (**e**) axial strain 7.0%–9.0%.

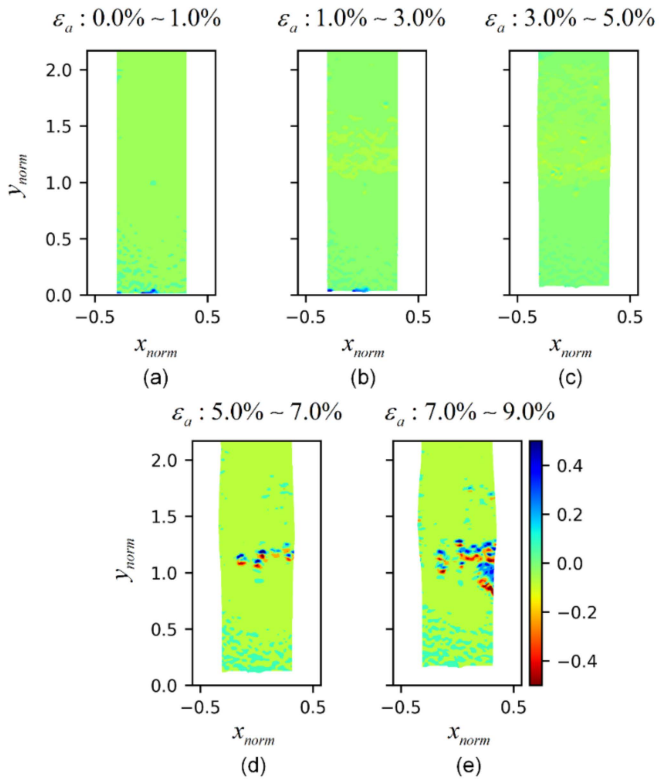

Figure 29. Evolution of gradient along $\hat{y}$ axis F_{33} of test 120704c: (**a**) axial strain 0.0%–1.0%; (**b**) axial strain 1.0%–3.0%; (**c**) axial strain 3.0%–5.0%; (**d**) axial strain 5.0%–7.0%; (**e**) axial strain 7.0%–9.0%.

5. Conclusions

A 3D spatio-temporal kinematic analysis was conducted on a series of triaxial sand specimens sheared under different experimental conditions. This was achieved by introducing 3D kinematic operators under the cylindrical coordinates, which can appropriately account for the specimen geometry. Kinematic results showed 3D micro- to meso-scale localization effects during shearing of the triaxial specimens, leading to the following conclusions:

(1) The development of expansion bands and compaction bands occurred at different temporal stages. Expansion bands were seen initiating as early as in the hardening stage. With strain, softening began to occur and the expanding rate gradually declined, whereas the compaction band began to emerge in the adjacent areas of the expansion band.

(2) When a shear band was fully formed, it could alter the radial deformation of the specimen according to the shape and orientation of the shear band(s). Furthermore, local axial strain become concentrated exclusively within the shear band.

(3) The localization effects were less evident when confinement was low, or when tests were conducted on the loose specimen. On the other hand, high confining pressure could lead to multiple shear bands progressing simultaneously.

(4) The kinematic characterization of the layered specimen showed a similar behavior to that of the loose specimen. Additionally, the failure mode was governed by the material response within the loose part of the specimen.

It is worth noting that stochastic behavior was present in the sand localization effects, driven by the heterogeneous nature of the material. A statistical characterization of localization effects, which can account for the main deformation mode and uncertainty associated with the kinematics of the sand, is thus significant for further evaluation of sand's localization phenomena, and of interest for calibration and simulation, among other numerical studies on sand failure mechanisms. A follow up paper will introduce a spatio-temporal statistical analysis of the same kinematic operators discussed in this paper.

Author Contributions: Conceptualization, Y.Z. and Z.M.-C.; data curation, Y.Z. and Z.M.-C.; funding acquisition, Z.M.-C.; investigation, Y.Z. and Z.M.-C.; methodology, Y.Z.; project administration, Y.Z. and Z.M.-C.; resources, Z.M.-C.; supervision, Z.M.-C.; validation, Y.Z. and Z.M.-C.; visualization, Y.Z.; writing—original draft, Y.Z.; writing—review & editing, Z.M.-C. All authors have read and agreed to the published version of the manuscript.

Funding: Work presented in this paper was sponsored by multiple agencies, including the National Science Foundation (NSF), Consejo Nacional de Ciencia y Tecnologia (CONACYT), and Texas A&M University (TAMU).

Institutional Review Board Statement: Not applicable.

Informed Consent Statement: Not applicable.

Data Availability Statement: The experimental data supporting the findings of this paper are provided along with the article and made available at the Texas Data Repository (https://dataverse.tdl.org/dataverse/SGL-MDPI-Topic-StochasticGeomechancis-ForwardModeling) (accessed on 1 August 2022). Additional queries may be directed to the corresponding author.

Conflicts of Interest: The authors declare no conflict of interest.

Appendix A. Gradient: Divergence, and Curl in Cylindrical Coordinates

Appendix A.1. The Nabla Operator ∇

The *gradient*, the *divergence*, and the *curl* are first-order kinematic operators acting on fields. The conventional way to express them is via a vector called *nabla*, whose components are partial derivatives with respect to certain coordinates system. For instance, in Cartesian coordinates, the *nabla* operator ∇ is defined as:

$$\nabla = \hat{i}\frac{\partial}{\partial x} + \hat{j}\frac{\partial}{\partial y} + \hat{k}\frac{\partial}{\partial z} \tag{A1}$$

Given that the *nabla* operator is a vector, we can conduct some vector operations, such as dot product and cross product, which leads to the concept of divergence and curl in Cartesian coordinates, as shown in Equations (A2) and (A3):

$$\nabla \cdot U = \frac{\partial U_x}{\partial x} + \frac{\partial U_y}{\partial y} + \frac{\partial U_z}{\partial z} \tag{A2}$$

$$\nabla \times U = \hat{i}(\frac{\partial U_z}{\partial y} - \frac{\partial U_y}{\partial z}) + \hat{j}(\frac{\partial U_x}{\partial z} - \frac{\partial U_z}{\partial x}) + \hat{k}(\frac{\partial U_y}{\partial x} - \frac{\partial U_x}{\partial y}) \tag{A3}$$

Appendix A.2. Coordinate Transformation

The transformations between cylindrical and Cartesian coordinates are:

$$Cartesian \rightarrow Cylindrical : \begin{Bmatrix} \rho = \sqrt{x^2 + y^2} \\ \phi = \arctan(y, x) \\ z = z \end{Bmatrix} \tag{A4}$$

$$Cylindrical \rightarrow Cartesian : \begin{Bmatrix} x = \rho\cos\phi \\ y = \rho\sin\phi \\ z = z \end{Bmatrix} \tag{A5}$$

The unit vector in the cylindrical coordinates are the functions of position. They point to radius, tangential, and vertical directions, respectively. The forward and inverse transformations of unit vectors between Cartesian and cylindrical coordinates are:

$$Cartesian \rightarrow Cylindrical : \begin{Bmatrix} \hat{\rho} = \hat{i}\cos\phi + \hat{j}\sin\phi \\ \hat{\phi} = -\hat{i}\sin\phi + \hat{j}\cos\phi \\ \hat{z} = \hat{k} \end{Bmatrix} \tag{A6}$$

$$Cylindrical \rightarrow Cartesian : \begin{Bmatrix} \hat{i} = \hat{r}\cos\phi - \hat{\phi}\sin\phi \\ \hat{j} = \hat{r}\sin\phi + \hat{\phi}\cos\phi \\ \hat{k} = \hat{z} \end{Bmatrix} \tag{A7}$$

If we calculate the derivatives of $\hat{\rho}$, $\hat{\phi}$, and $\hat{z}$ with respect to ρ, ϕ, and z, the only non-zeros terms are:

$$\frac{\partial\hat{\rho}}{\partial\phi} = -\hat{i}\sin\phi + \hat{j}\cos\phi = \hat{\phi} \tag{A8}$$

$$\frac{\partial\hat{\phi}}{\partial\phi} = -\hat{i}\cos\phi - \hat{j}\sin\phi = -\hat{\rho} \tag{A9}$$

These useful terms can simplify the derivation of Divergence and Curl under cylindrical coordinates.

Appendix A.3. The Nabla Operator in Cylindrical Coordinates

To express *nabla* operator ∇ in cylindrical coordinates, we must map the terms $\hat{i}\frac{\partial}{\partial x}$, $\hat{j}\frac{\partial}{\partial y}$, and $\hat{k}\frac{\partial}{\partial z}$ onto the terms $\hat{r}\frac{\partial}{\partial r}$, $\hat{\phi}\frac{\partial}{\partial\phi}$, and $\hat{z}\frac{\partial}{\partial z}$ that are defined in cylindrical coordinates $U(r,\phi,z)$. A direct approach is to use the chain rule and transformation relationships introduced above, namely,

$$\begin{aligned} \hat{\rho}\frac{\partial}{\partial\rho} &= (\hat{i}\cos\phi + \hat{j}\sin\phi)(\frac{\partial x}{\partial\rho}\frac{\partial}{\partial x} + \frac{\partial y}{\partial\rho}\frac{\partial}{\partial y}) \\ &= (\hat{i}\cos\phi + \hat{j}\sin\phi)(\cos\phi\frac{\partial}{\partial x} + \sin\phi\frac{\partial}{\partial y}) \\ &= \cos^2\phi\hat{i}\frac{\partial}{\partial x} + \sin\phi\cos\phi\hat{i}\frac{\partial}{\partial y} + \sin\phi\cos\phi\hat{j}\frac{\partial}{\partial x} + \sin^2\phi\hat{j}\frac{\partial}{\partial y} \end{aligned} \tag{A10}$$

$$\begin{aligned} \hat{\phi}\frac{\partial}{\partial\phi} &= (-\hat{i}\sin\phi + \hat{j}\cos\phi)(\frac{\partial x}{\partial\phi}\frac{\partial}{\partial x} + \frac{\partial y}{\partial\phi}\frac{\partial}{\partial y}) \\ &= (-\hat{i}\sin\phi + \hat{j}\cos\phi)(-\rho\sin\phi\frac{\partial}{\partial x} + \rho\cos\phi\frac{\partial}{\partial y}) \\ &= \rho\sin^2\phi\hat{i}\frac{\partial}{\partial x} - \rho\sin\phi\cos\phi\hat{i}\frac{\partial}{\partial y} - \rho\sin\phi\cos\phi\hat{j}\frac{\partial}{\partial x} + \rho\cos^2\phi\hat{j}\frac{\partial}{\partial y} \end{aligned} \tag{A11}$$

and

$$\hat{z}\frac{\partial}{\partial z} = \hat{k}\frac{\partial}{\partial z} \tag{A12}$$

Compare to Equation (A1), an intuitive attempt is to divide Equation (A11) by ρ, and add it to Equations (A10) and (A12), then,

$$\begin{aligned} \hat{\rho}\frac{\partial}{\partial\rho} + \frac{\hat{\phi}}{\rho}\frac{\partial}{\partial\phi} + \hat{z}\frac{\partial}{\partial z} &= (\sin^2\phi + \cos^2\phi)\hat{i}\frac{\partial}{\partial x} + (\sin^2\phi + \cos^2\phi)\hat{j}\frac{\partial}{\partial y} + \hat{k}\frac{\partial}{\partial z} \\ &= \hat{i}\frac{\partial}{\partial x} + \hat{j}\frac{\partial}{\partial y} + \hat{k}\frac{\partial}{\partial z} \end{aligned} \tag{A13}$$

Therefore, we have

$$\nabla = \hat{\rho}\frac{\partial}{\partial\rho} + \frac{\hat{\phi}}{\rho}\frac{\partial}{\partial\phi} + \hat{z}\frac{\partial}{\partial z} \tag{A14}$$

Appendix A.4. Divergence in Cylindrical Coordinates

It is similar to analyzing *divergence* in Cartesian coordinates; the *divergence* in Cartesian coordinates is carried out by computing the dot product of *nabla* operator ∇ and vector field $U(\rho, \phi, z)$ That is,

$$\begin{aligned}\nabla \cdot U = & \left(\hat{\rho}\frac{\partial}{\partial \rho} + \frac{\hat{\phi}}{\rho}\frac{\partial}{\partial \phi} + \hat{z}\frac{\partial}{\partial z}\right)\left(U_\rho \hat{\rho} + U_\phi \hat{\phi} + U_z \hat{z}\right) \\ & = \hat{\rho}\left(\hat{\rho}\frac{\partial U_\rho}{\partial \rho} + U_\rho \frac{\partial \hat{\rho}}{\partial \rho} + \hat{\phi}\frac{\partial U_\phi}{\partial \rho} + U_\phi \frac{\partial \hat{\phi}}{\partial \rho} + \hat{z}\frac{\partial U_z}{\partial \rho} + U_z \frac{\partial \hat{z}}{\partial \rho}\right) \\ & + \frac{\hat{\phi}}{\rho}\left(\hat{\rho}\frac{\partial U_\rho}{\partial \phi} + U_\rho \frac{\partial \hat{\rho}}{\partial \phi} + \hat{\phi}\frac{\partial U_\phi}{\partial \phi} + U_\phi \frac{\partial \hat{\phi}}{\partial \phi} + \hat{z}\frac{\partial U_z}{\partial \phi} + U_z \frac{\partial \hat{z}}{\partial \phi}\right) \\ & + \hat{z}\left(\hat{\rho}\frac{\partial U_\rho}{\partial z} + U_\rho \frac{\partial \hat{\rho}}{\partial z} + \hat{\phi}\frac{\partial U_\phi}{\partial z} + U_\phi \frac{\partial \hat{\phi}}{\partial z} + \hat{z}\frac{\partial U_z}{\partial z} + U_z \frac{\partial \hat{z}}{\partial z}\right)\end{aligned} \tag{A15}$$

Since $\hat{\rho}$, $\hat{\phi}$, and $\hat{z}$ are orthogonal unit vectors, the inner product between each two is 0 (self-inner product equals to 1). Together with Equations (A8) and (A9), we have

$$\begin{aligned}\nabla \cdot U = & \hat{\rho}\left(\hat{\rho}\frac{\partial U_\rho}{\partial \rho} + 0 + \hat{\phi}\frac{\partial U_\phi}{\partial \rho} + 0 + \hat{z}\frac{\partial U_z}{\partial \rho} + 0\right) \\ & + \frac{\hat{\phi}}{\rho}\left(\hat{\rho}\frac{\partial U_\rho}{\partial \phi} + U_\rho \hat{\phi} + \hat{\phi}\frac{\partial U_\phi}{\partial \phi} - U_\phi \hat{\rho} + \hat{z}\frac{\partial U_z}{\partial \phi} + 0\right) \\ & + \hat{z}\left(\hat{\rho}\frac{\partial U_\rho}{\partial z} + 0 + \hat{\phi}\frac{\partial U_\phi}{\partial z} + 0 + \hat{z}\frac{\partial U_z}{\partial z} + 0\right) \\ & = \left(\frac{\partial U_\rho}{\partial \rho} + \frac{U_\rho}{\rho}\right) + \frac{1}{\rho}\frac{\partial U_\phi}{\partial \phi} + \frac{\partial U_z}{\partial z} \\ & = \frac{1}{\rho}\frac{\partial}{\partial \rho}\left(U_\rho \cdot \rho\right) + \frac{1}{\rho}\frac{\partial U_\phi}{\partial \phi} + \frac{\partial U_z}{\partial z}\end{aligned} \tag{A16}$$

Appendix A.5. Curl in Cylindrical Coordinates

The calculation of *curl* follows the same method, as *divergence* calculated in cylindrical coordinates. The cross product is calculated between *nabla* operator ∇ and vector field $U(\rho, \phi, z)$.

$$\begin{aligned}\nabla \times U = & \left(\hat{\rho}\frac{\partial}{\partial \rho} + \frac{\hat{\phi}}{\rho}\frac{\partial}{\partial \phi} + \hat{z}\frac{\partial}{\partial z}\right) \times \left(U_\rho \hat{\rho} + U_\phi \hat{\phi} + U_z \hat{z}\right) \\ & = \hat{\rho} \times \left(\hat{\rho}\frac{\partial U_\rho}{\partial \rho} + U_\rho \frac{\partial \hat{\rho}}{\partial \rho} + \hat{\phi}\frac{\partial U_\phi}{\partial \rho} + U_\phi \frac{\partial \hat{\phi}}{\partial \rho} + \hat{z}\frac{\partial U_z}{\partial \rho} + U_z \frac{\partial \hat{z}}{\partial \rho}\right) \\ & + \frac{\hat{\phi}}{\rho} \times \left(\hat{\rho}\frac{\partial U_\rho}{\partial \phi} + U_\rho \frac{\partial \hat{\rho}}{\partial \phi} + \hat{\phi}\frac{\partial U_\phi}{\partial \phi} + U_\phi \frac{\partial \hat{\phi}}{\partial \phi} + \hat{z}\frac{\partial U_z}{\partial \phi} + U_z \frac{\partial \hat{z}}{\partial \phi}\right) \\ & + \hat{z} \times \left(\hat{\rho}\frac{\partial U_\rho}{\partial z} + U_\rho \frac{\partial \hat{\rho}}{\partial z} + \hat{\phi}\frac{\partial U_\phi}{\partial z} + U_\phi \frac{\partial \hat{\phi}}{\partial z} + \hat{z}\frac{\partial U_z}{\partial z} + U_z \frac{\partial \hat{z}}{\partial z}\right) \\ & = \hat{\rho} \times \left(\hat{\rho}\frac{\partial U_\rho}{\partial \rho} + 0 + \hat{\phi}\frac{\partial U_\phi}{\partial \rho} + 0 + \hat{z}\frac{\partial U_z}{\partial \rho} + 0\right) \\ & + \frac{\hat{\phi}}{\rho} \times \left(\hat{\rho}\frac{\partial U_\rho}{\partial \phi} + U_\rho \hat{\phi} + \hat{\phi}\frac{\partial U_\phi}{\partial \phi} - U_\phi \hat{\rho} + \hat{z}\frac{\partial U_z}{\partial \phi} + 0\right) \\ & + \hat{z} \times \left(\hat{\rho}\frac{\partial U_\rho}{\partial z} + 0 + \hat{\phi}\frac{\partial U_\phi}{\partial z} + 0 + \hat{z}\frac{\partial U_z}{\partial z} + 0\right) \\ & = \frac{\partial U_\phi}{\partial \rho}\hat{z} - \frac{\partial U_z}{\partial \rho}\hat{\phi} - \frac{1}{\rho}\frac{\partial U_\rho}{\partial \phi}\hat{z} + \frac{U_\phi}{\rho}\hat{z} + \frac{1}{\rho}\frac{\partial U_z}{\partial \phi}\hat{\rho} + \frac{\partial U_\rho}{\partial z}\hat{\phi} - \frac{\partial U_\phi}{\partial z}\hat{\rho} \\ & = \hat{\rho}\left(\frac{1}{\rho}\frac{\partial U_z}{\partial \phi} - \frac{\partial U_\phi}{\partial z}\right) + \hat{\phi}\left(\frac{\partial U_\rho}{\partial z} - \frac{\partial U_z}{\partial \rho}\right) + \hat{z}\left(\frac{1}{\rho}\frac{\partial}{\partial \rho}\left(V_\phi \cdot \rho\right) - \frac{1}{\rho}\frac{\partial U_\rho}{\partial \phi}\right)\end{aligned} \tag{A17}$$

Appendix A.6. Gradient in Cylindrical Coordinates

The *gradient* of a smooth vector field $U(\rho, \phi, z)$ in cylindrical coordinates is defined to be a second order tensor field,

$$\begin{aligned}
\nabla \otimes U = & \frac{\partial}{\partial \rho}\left(U_\rho \hat{\rho} + U_\phi \hat{\phi} + U_z \hat{z}\right) \otimes \hat{\rho} \\
& + \frac{\partial}{\partial \phi}\left(U_\rho \hat{\rho} + U_\phi \hat{\phi} + U_z \hat{z}\right) \otimes \frac{\hat{\phi}}{\rho} \\
& + \frac{\partial}{\partial z}\left(U_\rho \hat{\rho} + U_\phi \hat{\phi} + U_z \hat{z}\right) \otimes \hat{z} \\
& = \left(\frac{\partial U_\rho}{\partial \rho}\hat{\rho} + \frac{\partial U_\phi}{\partial \rho}\hat{\phi} + \frac{\partial U_z}{\partial \rho}\hat{z}\right) \otimes \hat{\rho} \\
& + \left(\frac{\partial U_\rho}{\partial \phi}\hat{\rho} + U_\rho \hat{\phi} + \frac{\partial U_\phi}{\partial \phi}\hat{\phi} - U_\phi \hat{\rho} + \frac{\partial U_z}{\partial \phi}\hat{z}\right) \otimes \frac{\hat{\phi}}{\rho} \\
& + \left(\frac{\partial U_\rho}{\partial z}\hat{\rho} + \frac{\partial U_\phi}{\partial z}\hat{\phi} + \frac{\partial U_z}{\partial z}\hat{z}\right) \otimes \hat{z} \\
& = \frac{\partial U_\rho}{\partial \rho}\hat{\rho} \otimes \hat{\rho} + \frac{\partial U_\phi}{\partial \rho}\hat{\phi} \otimes \hat{\rho} + \frac{\partial U_z}{\partial \rho}\hat{z} \otimes \hat{\rho} \\
& + \frac{1}{\rho}\left(\frac{\partial U_\rho}{\partial \phi} - U_\phi\right)\hat{\rho} \otimes \hat{\phi} + \frac{1}{\rho}\left(\frac{\partial U_\phi}{\partial \phi} + U_\rho\right)\hat{\phi} \otimes \hat{\phi} + \frac{1}{\rho}\frac{\partial U_z}{\partial \phi}\hat{z} \otimes \hat{\phi} \\
& + \frac{\partial U_\rho}{\partial z}\hat{\rho} \otimes \hat{z} + \frac{\partial U_\phi}{\partial z}\hat{\phi} \otimes \hat{z} + \frac{\partial U_z}{\partial z}\hat{z} \otimes \hat{z}
\end{aligned} \tag{A18}$$

or, in matrix form,

$$grad U = [\nabla \otimes U] = \begin{bmatrix} \frac{\partial U_\rho}{\partial \rho} & \frac{1}{\rho}\left(\frac{\partial U_\rho}{\partial \phi} - U_\phi\right) & \frac{\partial U_\rho}{\partial z} \\ \frac{\partial U_\phi}{\partial \rho} & \frac{1}{\rho}\left(\frac{\partial U_\phi}{\partial \phi} + U_\rho\right) & \frac{\partial U_\phi}{\partial z} \\ \frac{\partial U_z}{\partial \rho} & \frac{1}{\rho}\frac{\partial U_z}{\partial \phi} & \frac{\partial U_z}{\partial z} \end{bmatrix} \tag{A19}$$

References

1. Medina-Cetina, Z.; Song, A.; Zhu, Y.; Pineda-Contreras, A.R.; Rechenmacher, A. Global and Local Deformation Effects of Dry Vacuum-Consolidated Triaxial Compression Tests on Sand Specimens: Making a Database Available for the Calibration and Development of Forward Models. *Materials* **2022**, *15*, 1528. [CrossRef]
2. Zhu, Y.; Medina-Cetina, Z.; Pineda-Contreras, A.R. Spatio-Temporal Statistical Characterization of Boundary Kinematic Phenomena of Triaxial Sand Specimens. *Materials* **2022**, *15*, 2189. [CrossRef]
3. Borja, R.I. A Finite Element Model for Strain Localization Analysis of Strongly Discontinuous Fields Based on Standard Galerkin Approximation. *Comput. Methods Appl. Mech. Eng.* **2000**, *190*, 1529–1549. [CrossRef]
4. Andrade, J.E.; Borja, R.I. Capturing Strain Localization in Dense Sands with Random Density. *Int. J. Numer. Methods Eng.* **2006**, *67*, 1531–1564. [CrossRef]
5. Rechenmacher, A.L.; Finno, R.J. Digital Image Correlation to Evaluate ShearBanding in Dilative Sands. *Geotech. Test. J.* **2004**, *27*, 13–22. [CrossRef]
6. Cundall, P.A.; Strack, O.D.L. A Discrete Numerical Model for Granular Assemblies. *Geotechnique* **1979**, *29*, 47–65. [CrossRef]
7. Bardet, J.-P.; Proubet, J. Adaptative Dynamic Relaxation for Statics of Granular Materials. *Comput. Struct.* **1991**, *39*, 221–229. [CrossRef]
8. Alonso-Marroquin, F.; Vardoulakis, I.; Herrmann, H.J.; Weatherley, D.; Mora, P. Effect of Rolling on Dissipation in Fault Gouges. *Phys. Rev. E* **2006**, *74*, 31306. [CrossRef]
9. Jiang, M.J.; Yan, H.B.; Zhu, H.H.; Utili, S. Modeling Shear Behavior and Strain Localization in Cemented Sands by Two-Dimensional Distinct Element Method Analyses. *Comput. Geotech.* **2011**, *38*, 14–29. [CrossRef]
10. Mohamed, A.; Gutierrez, M. Comprehensive Study of the Effects of Rolling Resistance on the Stress—Strain and Strain Localization Behavior of Granular Materials. *Granul. Matter* **2010**, *12*, 527–541. [CrossRef]
11. Ng, T.-T. Numerical Simulations of Granular Soil Using Elliptical Particles. *Comput. Geotech.* **1994**, *16*, 153–169. [CrossRef]
12. Oda, M.; Iwashita, K. Study on Couple Stress and Shear Band Development in Granular Media Based on Numerical Simulation Analyses. *Int. J. Eng. Sci.* **2000**, *38*, 1713–1740. [CrossRef]

13. Koenders, M.A.; Gaspar, N.; Tüzün, U. The Physical Effects of Structures Formation in Granular Materials. *Phys. Chem. Earth Part A Solid Earth Geod.* **2001**, *26*, 75–82. [CrossRef]
14. Williams, J.R.; Rege, N. Coherent Vortex Structures in Deforming Granular Materials. *Mech. Cohesive-Frict. Mater.* **1997**, *2*, 223–236. [CrossRef]
15. Cil, M.B.; Alshibli, K.A. 3D Analysis of Kinematic Behavior of Granular Materials in Triaxial Testing Using DEM with Flexible Membrane Boundary. *Acta Geotech.* **2014**, *9*, 287–298. [CrossRef]
16. Kawamoto, R.; Andò, E.; Viggiani, G.; Andrade, J.E. All You Need Is Shape: Predicting Shear Banding in Sand with LS-DEM. *J. Mech. Phys. Solids* **2018**, *111*, 375–392. [CrossRef]
17. Hall, S.A.; Bornert, M.; Desrues, J.; Pannier, Y.; Lenoir, N.; Viggiani, G.; Bésuelle, P. Discrete and Continuum Analysis of Localised Deformation in Sand Using X-Ray MCT and Volumetric Digital Image Correlation. *Géotechnique* **2010**, *60*, 315–322. [CrossRef]
18. Andò, E.; Hall, S.A.; Viggiani, G.; Desrues, J.; Bésuelle, P. Grain-Scale Experimental Investigation of Localised Deformation in Sand: A Discrete Particle Tracking Approach. *Acta Geotech.* **2012**, *7*, 1–13. [CrossRef]
19. Amirrahmat, S.; Druckrey, A.M.; Alshibli, K.A.; Al-Raoush, R.I. Micro Shear Bands: Precursor for Strain Localization in Sheared Granular Materials. *J. Geotech. Geoenviron, Eng.* **2019**, *145*, 1–18. [CrossRef]
20. Alshibli, K.A.; Jarrar, M.F.; Druckrey, A.M.; Al-Raoush, R.I. Influence of Particle Morphology on 3D Kinematic Behavior and Strain Localization of Sheared Sand. *J. Geotech. Geoenviron. Eng.* **2016**, *143*, 04016097. [CrossRef]
21. Desrues, J.; Andò, E. Strain Localisation in Granular Media. *C. R. Phys.* **2015**, *16*, 26–36. [CrossRef]
22. Druckrey, A.M.; Alshibli, K.A.; Al-Raoush, R.I. Discrete Particle Translation Gradient Concept to Expose Strain Localisation in Sheared Granular Materials Using 3D Experimental Kinematic Measurements. *Geotechnique* **2018**, *68*, 162–170. [CrossRef]
23. Amirrahmat, S.; Alshibli, K.A.; Jarrar, M.F.; Zhang, B.; Regueiro, R.A. Equivalent Continuum Strain Calculations Based on 3D Particle Kinematic Measurements of Sand. *Int. J. Numer. Anal. Methods Geomech.* **2018**, *42*, 999–1015. [CrossRef]
24. Liu, J.; Iskander, M. Adaptive Cross Correlation for Imaging Displacements in Soils. *J. Comput. Civ. Eng.* **2004**, *18*, 46–57. [CrossRef]
25. Song, A. Deformation Analysis of Sand Specimens Using 3D Digital Image Correlation for the Calibration of an Elasto-Plastic Model. Ph.D. Thesis, Texas A&M University, College Station, TX, USA, 2012.
26. Rechenmacher, A.; Abedi, S.; Chupin, O. Evolution of Force Chains in Shear Bands in Sands. *Géotechnique* **2010**, *60*, 343–351. [CrossRef]
27. Rechenmacher, A.L.; Abedi, S.; Chupin, O.; Orlando, A.D. Characterization of Mesoscale Instabilities in Localized Granular Shear Using Digital Image Correlation. *Acta Geotech.* **2011**, *6*, 205–217. [CrossRef]
28. Abedi, S.; Rechenmacher, A.L.; Orlando, A.D. Vortex Formation and Dissolution in Sheared Sands. *Granul. Matter* **2012**, *14*, 695–705. [CrossRef]
29. Medina-Cetina, Z.; Rechenmacher, A. Influence of Boundary Conditions, Specimen Geometry and Material Heterogeneity on Model Calibration from Triaxial Tests. *Int. J. Numer. Anal. Methods Geomech.* **2010**, *34*, 627–643. [CrossRef]
30. Sutton, M.A.; Yan, J.H.; Tiwari, V.; Schreier, H.W.; Orteu, J.-J. The Effect of Out-of-Plane Motion on 2D and 3D Digital Image Correlation Measurements. *Opt. Lasers Eng.* **2008**, *46*, 746–757. [CrossRef]
31. Correlated Solution. Available online: https://www.correlatedsolutions.com/ (accessed on 1 August 2022).
32. Sutton, M.A.; McNeill, S.R.; Helm, J.D.; Chao, Y.J. Advances in Two-Dimensional and Three-Dimensional Computer Vision. In *Photomechanics*; Springer: Berlin/Heidelberg, Germany, 2000; pp. 323–372.
33. Medina-Cetina, Z. Probabilistic Calibration of a Soil Model. Ph.D. Thesis, The John Hopkins University, Baltimore, MD, USA, 2006.
34. Rechenmacher, A.L. Grain-Scale Processes Governing Shear Band Initiation and Evolution in Sands. *J. Mech. Phys. Solids* **2006**, *54*, 22–45. [CrossRef]
35. Desrues, J.; Chambon, R.; Mokni, M.; Mazerolle, F. Void Ratio Evolution inside Shear Bands in Triaxial Sand Specimens Studied by Computed Tomography. *Géotechnique* **1996**, *46*, 529–546. [CrossRef]
36. Gurtin, M.E. *An Introduction to Continuum Mechanics*; Academic Press: New York, NY, USA, 1982.
37. Oda, M.; Kazama, H. Microstructure of Shear Bands and Its Relation to the Mechanisms of Dilatancy and Failure of Dense Granular Soils. *Géotechnique* **1998**, *48*, 465–481. [CrossRef]
38. Liu, B.; Kong, L.; Li, C.; Wang, J. Evolution of Shear Band in Plane Strain Compression of Naturally Structured Clay with a High Sensitivity. *Appl. Sci.* **2022**, *12*, 1180. [CrossRef]